

AD\_\_\_\_\_

Award Number: W81XWH-04-1-0042

TITLE: Transurethral Ultrasound Diffraction Tomography

PRINCIPAL INVESTIGATOR: Matthias C. Schabel, Ph.D.

CONTRACTING ORGANIZATION: University of Utah  
Salt Lake City, UT 84108

REPORT DATE: March 2007

TYPE OF REPORT: Final

PREPARED FOR: U.S. Army Medical Research and Materiel Command  
Fort Detrick, Maryland 21702-5012

DISTRIBUTION STATEMENT: Approved for Public Release;  
Distribution Unlimited

The views, opinions and/or findings contained in this report are those of the author(s) and should not be construed as an official Department of the Army position, policy or decision unless so designated by other documentation.

REPORT DOCUMENTATION PAGE				Form Approved OMB No. 0704-0188	
Public reporting burden for this collection of information is estimated to average 1 hour per response, including the time for reviewing instructions, searching existing data sources, gathering and maintaining the data needed, and completing and reviewing this collection of information. Send comments regarding this burden estimate or any other aspect of this collection of information, including suggestions for reducing this burden to Department of Defense, Washington Headquarters Services, Directorate for Information Operations and Reports (0704-0188), 1215 Jefferson Davis Highway, Suite 1204, Arlington, VA 22202-4302. Respondents should be aware that notwithstanding any other provision of law, no person shall be subject to any penalty for failing to comply with a collection of information if it does not display a currently valid OMB control number. <b>PLEASE DO NOT RETURN YOUR FORM TO THE ABOVE ADDRESS.</b>					
1. REPORT DATE (DD-MM-YYYY) 01/03/07		2. REPORT TYPE Final		3. DATES COVERED (From - To) 1 Mar 2004 – 28 Feb 2007	
4. TITLE AND SUBTITLE  Transurethral Ultrasound Diffraction Tomography				5a. CONTRACT NUMBER	
				5b. GRANT NUMBER W81XWH-04-1-0042	
				5c. PROGRAM ELEMENT NUMBER	
6. AUTHOR(S) Matthias C. Schabel, Ph.D.  E-Mail: <a href="mailto:mathis.schabel@hsc.utah.edu">mathis.schabel@hsc.utah.edu</a>				5d. PROJECT NUMBER	
				5e. TASK NUMBER	
				5f. WORK UNIT NUMBER	
7. PERFORMING ORGANIZATION NAME(S) AND ADDRESS(ES)  University of Utah Salt Lake City, UT 84108				8. PERFORMING ORGANIZATION REPORT NUMBER	
9. SPONSORING / MONITORING AGENCY NAME(S) AND ADDRESS(ES) U.S. Army Medical Research and Materiel Command Fort Detrick, Maryland 21702-5012				10. SPONSOR/MONITOR'S ACRONYM(S)	
				11. SPONSOR/MONITOR'S REPORT NUMBER(S)	
12. DISTRIBUTION / AVAILABILITY STATEMENT Approved for Public Release; Distribution Unlimited					
13. SUPPLEMENTARY NOTES					
14. ABSTRACT: The potential for cost-effective tomographic imaging using ultrasound continues to be confronted with difficulties arising from the computational complexity of fully three-dimensional object reconstruction in the diffraction regime. Development of fast and accurate forward and inverse models for ultrasound propagation in the biomedical frequency range of 1-10 MHz is essential for diffraction tomography to be a practical imaging modality. We have implemented a flexible, object-oriented simulation system in MATLAB for performing rapid two- and three-dimensional modeling of forward scattering using the conjugate gradient FFT method in conjunction with a fast linear adjoint approximation to the Jacobian. Nonlinear conjugate gradient inversion has been implemented and tested in both 2D and 3D, demonstrating the feasibility of the method for diffraction tomography. We have also implemented and tested several regularization schemes including L2-norm and total variation, and have used multigrid iteration in conjunction with anisotropic diffusion filtering to accelerate convergence of the inversion algorithm. Inversions of strongly scattering objects have been successfully performed in 2D and 3D, and results					
15. SUBJECT TERMS acoustic inverse scattering, acoustic tomography, Lippmann-Schwinger Equation, conjugate gradient FFT, prostate imaging					
16. SECURITY CLASSIFICATION OF:			17. LIMITATION OF ABSTRACT	18. NUMBER OF PAGES	19a. NAME OF RESPONSIBLE PERSON
a. REPORT	b. ABSTRACT	c. THIS PAGE			USAMRMC
U	U	U	UU	48	19b. TELEPHONE NUMBER (include area code)

**Transurethral Ultrasound Diffraction  
Tomography**  
Final Report for Award Number  
W81XWH-04-1-0042

Matthias C. Schabel, Ph.D.      Dilip Ghosh Roy, Ph.D.

March 1, 2006 - February 28, 2007

# Contents

1	Introduction	2
2	Preconditioning	3
3	Contrast-Source Inversion (CSI)	4
4	Acquiring Experimental Data	7
5	Parallelization of the Forward Model	8
6	Noise Propagation in Inverse Scattering	8
7	Acoustic Emission from an IVUS Transducer	8
8	Key Research Accomplishments	9
9	Reportable Outcomes	11
10	Conclusions and Future Work	12
11	Figures	14

# 1 Introduction

The primary objective of this project has been to develop effective ultrasonic tomographic algorithms that are applicable to the endoluminal geometry found in prostate imaging. The method of reconstruction is that of inverse scattering in which an unknown scatterer is recovered from the knowledge of the fields scattered by the object in an appropriately designed scattering geometry. It was mentioned in our previous reports, that inverse scattering is capable of overcoming the two major limitations of conventional ultrasound imaging, namely, its non-quantitativeness, subjectivity and sensitivity to speckle noise arising from multiple scattering of acoustic wave radiation. However, numerous challenges remain before inverse scattering ultrasonic tomography becomes feasible in real-world applications. It is well-known that ultrasound tomography in inverse scattering is mathematically complex, computationally intensive, and like any inverse solution of a physical problem, ill-posed.[1, 3] In the previous report, we demonstrated how the ill-posedness could be overcome by using regularization, appropriate data sets and reconstruction techniques. Toward that a multi-wave, multi-frequency data set was used in Tikhonov regularization with a particularly chosen  $L_2$ -norm in the object error. Moreover, the reconstructions were performed by stepping up in grid sizes instead of computing with the full grid size all at once. We demonstrated improved convergence using frequency hopping multigrid inversion, and showed that it was possible to overcome the problem of the local minima and improve inversion performance using this approach. Furthermore, the regularizing character inherent in multi-gridding was also demonstrated in the previous report. A further significant gain in computational speed was achieved by using the adjoint fields to calculate the gradient of the objective function eliminating thereby the computationally intractable task of having to determine the full Jacobian matrix. The application of inverse scattering ultrasonic tomography in quantitative tissue imaging was convincingly demonstrated in our last progress report via the reconstructions 2-D and 3-D Shepp-Logan tissue phantoms by nonlinear conjugate gradient method on the basis of multi-incident, multi-frequency data and multi-grid reconstruction. In addition, the feasibility of the technique was further tested by reconstructing, in addition to the tissue phantoms, a stylized endoluminal geometry, and it was done in two different scattering geometries - the usual exterior/exterior geometry and a novel exterior/interior or semi-endoluminal scattering configuration which was specially designed

with a view to transurethral application.

In the final year of this project, we have continued to address the issue of accelerating inversion performance. This work has focused on implementation of a preconditioning scheme for accelerating convergence of the conjugate gradient minimization algorithm, developing and coding a fast contrast-source inversion algorithm to provide an improved initial guess at the scattering object, and design and implementation of a scheme for parallel computation of the forward model using the Message Passing Interface (MPI). We have also recently developed a collaboration with a company producing a commercial scanner for ultrasound tomography (in the exterior/exterior geometry) and have begun to test our reconstruction algorithms using test data. We have also developed a theoretical analysis of noise propagation in inverse scattering (attached in Appendix A), analyzed acoustical wave propagation in circular ducts of various wall conditions in the presence of flow (attached in Appendix B), and investigated transmitted acoustic field patterns for catheter-based IVUS transmitters.

## 2 Preconditioning

As regarding the solution to the problem of the computational complexity of inverse scattering tomography in imaging the prostate (or any tissue complex and/or endoluminal anatomy, for that matter), two recourses are available in general: parallel computing and designing a suitable preconditioner. Both are discussed in this report, beginning with the preconditioner first. However, in view of the complexity of the matrix mathematics that is involved in the preconditioner calculation, only the basic outlines and the final results are given.

The preconditioner described here is based upon the seminal work of Hohage.[7] The basic idea behind the preconditioner is to combine the well-known *Lanczos algorithm*[4] for calculating the eigenvalues of a matrix (via tri-diagonalization), and the orthogonal sequences of the conjugate directions that are generated during the iterations (NLCG iteration in this project). The first step in the design of the preconditioner is to transform the variational problem (detailed in the previous two reports) into normal equations. It involves transforming the objective functional (that was minimized) into the form:  $\mathcal{F}_n^T \mathcal{F}_n = F'_n(\gamma^*)^T F'_n(\gamma^*) + \alpha_n I$ .  $F'$  is the Fréchet derivative of the functional with respect to the unknown object  $\gamma$ , and  $\alpha_n$  is an iteratively

updated regularization parameter.  $I$  is the identity matrix, the superscript  $T$  denotes the transpose operation, and  $n$  is the stage of iteration.

The preconditioner is obtained from the eigenvalues and eigenfunctions of the normal, symmetrical matrix,  $F'_n(\gamma^*)^T F'_n(\gamma^*)n$ . Let  $\{v_j, \lambda_j, \lambda_1 \geq \lambda_2 \geq \lambda_3 \dots\}$  be the eigenvalues and eigenfunctions. Let  $\mathbf{r}$  be the orthonormalized conjugate direction vector that is generated within the CGNE routine, and  $\mathbf{q}$  the vector which appears in the object (in NLCG) or in the Newton step (in the case of the Newton method) update. In other words,  $\chi_{n+1} = \chi_n + \alpha_n \mathcal{F}_n^{-1} \mathbf{q}$ ,  $n$  being the stage of iteration. The Lanczos tri-diagonal matrix is built from  $\mathbf{r}$  and  $\mathbf{q}$  vectors. The actual computation of the spectrum of this tri-diagonal matrix can be accomplished by any of the available robust method for the purpose such as the QR-decomposition.[4] The preconditioner,  $P$ , takes the form:

$$P_n x = \alpha_n x + \sum_{j=1}^k \lambda_j (x, v_j) v_j,$$

from which it follows that

$$P_n^{-1} y = \frac{1}{\alpha_n} y + \sum_{j=1}^k \left( \frac{1}{\alpha_n + \lambda_j} - \frac{1}{\alpha_n} \right).$$

### 3 Contrast-Source Inversion (CSI)

In our last report, mention was made of the CSI method. We have finished writing the MATLAB code for multidimensional CSI reconstruction using multifrequency, multi-wave data. There are two components in CSI, namely, the source and the object. Although the two are interdependent, their updates can be performed separately. With the following definitions :

$\text{scat}$  = the data vector.

$C_1 = \text{norm}(\text{scat})^2$ .

$\gamma_0$  = the initial estimate of the object obtained by weighted backpropagating of the measured data.

$\gamma$  = the reconstructed object.

$w_{jn}$  = the equivalent source in the  $j$ -th incidence and in the  $n$ -th stage of iteration.

$u_{jn}$  = the total field corresponding to  $w_{jn}$ .

$u_j^{inc}$  = the incident field.

$\rho_{jn}$  = the data discrepancy in the j-th incidence and in the n-th stage of iteration.

$r_{jn}$  = the object discrepancy in the j-th incidence and in the n-th stage of iteration.

$G_D$  = Green's function in the computational domain.

$G_S$  = Green's function in the detector domain.

$g_{jn}^w$  = gradient in the w-update.

$\ell_{wn}$  = steplength in the update of the Polak-Ribière conjugate directions for w.

$v_{jn}$  = conjugate directions in the linear conjugate gradient iteration for w.

$\alpha_{wn}$  = steplength in the update of w.

$g_n^\gamma$  = gradient in the object-update.

$\ell_{\gamma n}$  = steplength in the update of the Polak-Ribière conjugate directions for the object.

$d_n^\gamma$  = conjugate directions in the linear conjugate gradient iteration for the object.

$\alpha_{\gamma n}$  = steplength in the update of the object.

$*$  = the operation of convolution.

CD = the computational domain.

DD = the detector domain.

$(\cdot, \cdot)_Y$  = the inner product on Y.

$\sum'$  = sum over j and n.

$\bar{z}$  = the complex conjugate of z.

our implementation of CSI is as follows:

The Source Update:



$$\begin{aligned}
C_{2,n-1} &= \left\{ \sum' |\gamma_{n-1} u_j^{inc}|^2 \right\}. \\
u_{j,n+1} &= u_j^{inc} + G_D * w_{jn}. \\
w_{j,n+1} &= w_{jn} + \alpha_{jn} v_{jn}. \\
v_{jn} &= g_{jn}^w + \ell_{wn} \alpha_{wn}. \\
\ell_{wn} &= \frac{Re \sum' \langle g_{jn}^w, g_{jn}^w - g_{j,n-1}^w \rangle_{CD}}{\langle g_{j,n-1}^w, g_{j,n-1}^w \rangle_{CD}}. \\
\alpha_{wn} &= -\frac{\langle g_{jn}^w, v_{jn} \rangle_{CD}}{C_1 (norm(G_S v_{jn}))^2 + C_{2,n-1} (norm(v_{jn} - \gamma_{n-1} G_D v_{jn}))^2}. \\
g_{jn}^\gamma &= -[C_1^2 \bar{G}_S \rho_{j,n-1} + C_{2,n-1} \{I - \bar{G}_D \bar{\gamma}_{n-1}\} r_{j,n-1}].
\end{aligned}$$

The Contrast Update:

$$\begin{aligned}
g_n^\gamma &= C_{2,n-1} \left( \frac{\sum_j w_{jn} \bar{u}_{jn}}{\sum_j |u_{jn}|^2} - \gamma_{n-1} \right). \\
d_n &= g_n^\gamma + \ell_{\gamma n} d_{n-1}. \\
\ell_{\gamma n} &= \frac{Re \sum \langle g_n^\gamma, g_n^\gamma - g_{n-1}^\gamma \rangle_{CD}}{\langle g_{n-1}^\gamma, g_{n-1}^\gamma \rangle_{CD}}. \\
\gamma_{n+1} &= \gamma_n + \alpha_{\gamma n} d_n.
\end{aligned}$$

The Polak-Ribière steplength,  $\alpha_{\gamma n}$ , is a highly involved expression containing the current updates in both the source and the contrast quantities, and its explicit expression is not given here. We applied the CSI algorithm to multifrequency data, but upsampling in frequency.

The backpropagated CSI image was incorporated into the NLGC routine showing a slight reduction in the number of iterations. This suggests that a correctly reconstructed CSI image (which is, as already mentioned, is quite fast) as an input to the NLGC iteration would lead to faster convergence.

## 4 Acquiring Experimental Data

Only recently, we have succeeded in gaining access to a commercial scanner which can be used to generate experimental data. The scanner is owned by a locally based breast imaging company, Techniscan Medical Systems, Inc. As of now, Techniscan's scanner operates in the transmission mode. However, it is soon to be modified for reflection mode imaging which is what is required for prostate imaging. We have already acquired some trial run, transmission mode data. The details of the Techniscan scanner in which the data were acquired is shown in Figure 1.[9]. It is essentially a confocal geometry in which two-dimensional, slice-by-slice,  $180^\circ$  data can be collected in the temporal as well as in the frequency domain. The data that we acquired were the frequency domain data. Figure 1. Techniscan Medical's ultrasonic scanner geometry. (a) The  $128 \text{ mm} \times 16 \text{ mm}$  receiver array. There are 6 rows and 160 columns, i.e., 960 elements total. The central two rows are 4.6 mm each. The next outer two rows are 1.9 mm each, whereas the rest two rows are 1.45 mm each. (b) The plan view of the scanner. The entire system is immersed in a water bath. The transmitter-receiver system rotate together around an axis. The measurements are made at every  $2^\circ$  of rotation. (c) The focussing arrangement. Both the transmitter and the receiver are focussed with a focal length of 60 mm.

Figure 1(a) shows the details of the scanner's receiver array. The array has 960 receiving elements. The length of the array is 128 mm and its width is 16 mm containing 6 rows. The central two rows are each of width 4.6 mm, the adjacent two are 1.9 mm wide each, whereas the outermost 2 rows are each 1.45 mm wide. The transmitter which has the length of 140 mm and width of 16 mm, is made from a single piece. Figure 1(b) is the plan view of the scanner showing the organ (scatterer) between the transmitter and the receiver, the entire arrangement being immersed in a water bath. In order to acquire two-dimensional slices at discrete "levels", that is, at various heights in the object (a prostate phantom, for example), the transmitter and the receiver are both focussed (focal length = 60 mm), as shown in Figure 1(c), which displays the view of the elevation. The data are first acquired by rotating the transmitter-receiver system around the scatterer. The measurements are made at every  $2^\circ$  of rotation. Because of the focusing arrangement, approximate 2-D data at any pre-set level can be obtained by simply summing over the six bins of the receiver array in Figure 1(a), that is, along the width of the array. The time domain data are acquired by chirping the transmitter. These are then

Fourier transformed into the frequency domain data. The clock rate is 33 MHz, and the FFT is performed after 1536 time intervals.

## 5 Parallelization of the Forward Model

For realistic imaging geometries, it is expected that anywhere from 64-256 incident waves and a corresponding number of detectors will be used in the image reconstruction system.

## 6 Noise Propagation in Inverse Scattering

The propagation of noise from the detectors to the image via the reconstruction algorithm was investigated. The algorithm in this project was:  $\nabla_{\gamma}\Phi = Re[\psi\psi^+] = 0$ . Expressions for the covariance matrix was derived. The covariance reduced to that of the X-ray CT under the assumptions of linear operator and real data.[5] The analytical covariance matrix was further specialized to the limit of the Born approximation. The variance in the Born image pixels was found to be constant, while the covariance at a pixel was highly peaked and decayed oscillatorily away from the pixel. These findings were in agreement with the results obtained by the direct Born calculations. Further details are presented in ??.

## 7 Acoustic Emission from an IVUS Transducer

In the last progress report, some calculations were presented regarding the characteristics of the fields emitted by a catheter-based miniature transmitter. For transurethral imaging of the prostate gland, the knowledge of the characteristics of such transmitters is of interest. Some results of numerical computations are shown in Figures 2. In this figure, a miniaturized emitter is situated on the cylindrical surface of the catheter, the diameter of which is 3 F. The emitter has a total angular width of  $0.375^\circ$ . The wavenumber  $k_0 = 50$ . For the Robin or the impedance catheter, the wall admittance in the plots shown is real and its value is 15. The plots are representatives of the emitted fields.

Figure 2(a) results if the catheter surface is a Neumann surface, whereas Figure 2(b) shows the results for a Robin or impedance catheter. The fields emitted by a transmitter in an unbounded space are shown in Figure 2(c). A comparison between Figures 2(a) and 2(b) with Figure 2(c) clearly shows that the fields of the catheter-based transmitters are more directional than the transmitter in the unbounded medium. The latter is an isotropic emitter as opposed to the catheter-based ones. The objective is to understand if a two-dimensional, slice-by-slice imaging is possible with the miniature transmitters. Further studies are, however, needed for a definitive answer.

## 8 Key Research Accomplishments

The central objective of the project was to develop methods for imaging internal anatomies with an emphasis on imaging tissue complexes such as the prostate gland by quantitative ultrasound so that some of the deficiencies of conventional ultrasound imaging could be removed. Inverse scattering in ultrasonic frequencies was proposed as the method of choice. Two key issues are involved in the implementation of any ultrasonic inverse scattering algorithm. These are: (1) efficient solutions of the Lippmann-Schwinger integral equation of scattering - the so-called forward problem, and (2) the speed of the numerical inversions. The latter in turn includes the problem of fast computation of the gradient, negotiation of the local minima, and general imaging protocols for gaining advantage in speed. The project accomplishments are summarized below.

- Fast and efficient codes for the solution of the Lippmann-Schwinger equation were written using CG-FFT. These were checked against analytical benchmark solutions. Our numerical results were found to have a negligible error of about only 0.4 percent. It was a convincing demonstration of the efficacy and accuracy of the numerical codes which were developed in this project for solving the forward problems in 2-D and in 3-D.
- For inversions, multi-frequency data were used in order to minimize the problem of the local minima. Moreover, the adjoint fields which were used in the calculation of the gradient of the objective functional, led to a significant reduction in computations. Only one extra forward problem (per incidence) needed to be solved in this technique. The

gradient, calculated by the method of adjoint fields, resulted in almost identical results when compared against the brute force finite difference calculations.

- The multigrid bootstrapping approach yielded relatively speedier reconstructions.
- An exterior-interior or semi-endoluminal configuration was introduced and investigated for intra-organ reconstructions during the course of this project. It is an entirely novel scattering geometry which is expected to be useful for imaging any internal tissue anatomy as well as imaging the lumen of a vessel.
- The feasibility of the imaging procedures that were proposed and developed, including the new semi-endoluminal configuration, were convincingly demonstrated by numerically reconstructing Shepp-Logan tissue phantoms and stylized endoluminal phantoms in both 2-D and in 3-D. In addition, the strength of the scatterer as high as  $\gamma_{max} = 0.3$ , that is, allowing for as much as 30 percent variation in the speed of sound relative to the background. It is well beyond the Born limit.
- As an important contribution, we have outlined a preconditioner that was first proposed by Hohage for the Newton methods using normal equations. The preconditioner led to orders of magnitude gain in the speed of the inversions. We have proposed the use of Hohage's preconditioner for the NLCG iterations, as were done in this project.
- We have written MATLAB code for rapid inversions by the Contrast-Source-Inversion (CSI) technique that uses the preconditioned gradient and only linear CG. All expressions in CSI are analytical, and the method yields quite rapid inversions. However, our purpose is to use the basic CSI in a bootstrapped frequency and upsampling to accelerate convergence and improve accuracy of our reconstructions.
- An arrangement was made with Techniscan Medical Systems, Inc., Salt Lake City, Utah, for using its scanner for acquiring experimental patient data. Techniscan specializes in breast tumor imaging. Both temporal and spectral data can be obtained. We have already acquired frequency domain data acquired *in vivo* in the human breast and have begun tests of our algorithm using this data.

- A scheme of a parallel computation for accelerating the solution of the inverse problem has been developed and implemented using MPI. This approach facilitates the use of widely available computational clusters (MIMD) supporting this standard protocol. While communication overhead limits performance for small grid sizes, this becomes relatively unimportant
- Numerical results have been obtained for the transmitted acoustic fields of catheter-based IVUS transducers.
- Novel theoretical results on noise propagation in inverse scattering using the adjoint field gradient have been developed.
- Peripheral to the investigation of semi-endoluminal scattering, the characteristics of propagation of acoustic waves in cylindrical waveguides for various types of wall conditions were investigated both theoretically and numerically.

## 9 Reportable Outcomes

The accomplishments cited above have been translated into an invited lecture, a refereed journal publication, and one paper submitted to a peer-reviewed journal, and one paper in preparation for submission to a peer-reviewed journal:

- DN Ghosh Roy, John Roberts, Matthias Schabel and SJ Norton, Noise propagation in linear and nonlinear inverse scattering, *J. Acous. Soc. Am.*, vol. 125, May 2007.
- DN Ghosh Roy, John Roberts and Matthias Schabel, Acoustic wave propagation in a cylindrical waveguide in the presence of flow, submitted to *J. Sound and Vibration*.
- Matthias Schabel and DN Ghosh Roy, Two and three dimensional ultrasound tomography in exterior and semi-endoluminal geometry, in preparation for submission to *Physics in Medicine and Biology*.
- DN Ghosh Roy, John Roberts, Matthias Schabel and SJ Norton, *The Method of Adjoint Field in Inverse Scattering of Plane Waves*, Invited

Talk delivered at the Acoustical Society of America Annual Convention,  
Providence RI, June 2006.

## 10 Conclusions and Future Work

This project set an ambitious research plan; while not every proposed element of the work detailed in the initial grant submission has been fully achieved, we have made substantial progress on a number of fronts. In particular, we have developed and implemented code for performing full-wave acoustic inversion that is functions in 2D and 3D and for both the exterior-exterior and exterior-interior source/detector geometries. We have demonstrated the feasibility of frequency hopping as a means of eliminating the need for empirical regularization of the inversion algorithm and have demonstrated the ability to reconstruct large objects in the presence of simulated noise with excellent fidelity (up to grid sizes of  $256 \times 256$  in 2D and  $40 \times 40 \times 40$  in 3D). Computation time for reconstruction remains a challenge.

## References

- [1] D. Colton and R. Kress: *Inverse Acoustic and Electromagnetic Scattering Theory*, Springer-Verlag, 1992.
- [2] S.W. DEng and O.K. Ersoy, Parallel, self-organizing hierarchical neural networks with forward-backward training, J. Circuits Syst. Signal Process. (January 1993), pp. 23-246. vol.
- [3] D.N. Ghosh Roy and L. Couchman: *Inverse Problems and Inverse Scattering of Plane Waves*, Academic Press, 2002.
- [4] G.H. Golub and C.F. van Loan, *Matrix Computations*, Johns Hopkins University Press, 1989.
- [5] G.T. Gullberg, R.H. Huesman, D.N.G. Roy, J. Qi and B.W. Reutter, Estimation of the parameter covariance matrix for a one-compartment cardiac perfusion model estimated from a dynamic sequence reconstructed using map iterative reconstruction algorithms, IEEE Nuclear Science Symposium and Medical Imaging Conference Record, pp. 3019-3023, 2003.
- [6] S. Haykin, *Adaptive Filter Theory*, Prentice-Hall, 1986.
- [7] T. Hohage: On the numerical solution of a three-dimensional inverse medium scattering problem, Inverse Problems, vol. 17, pp. 1743-1763, 2001.
- [8] M. Kartal. B. Yazgan and O.K. Ersoy, Multistage parallel algorithm for diffraction tomography, *Applied Optica*, vol. 34, pp. 1426-1431, 1995.
- [9] J. Wiskin, D.T. Borup, S.A. Johnson, M. Berggren, T. Abbott and R. Hanover, Full-wave, non-linear, inverse scattering, *Acoustical Imaging*, vol. 28, pp. 183-193, 2007.



## 11 Figures

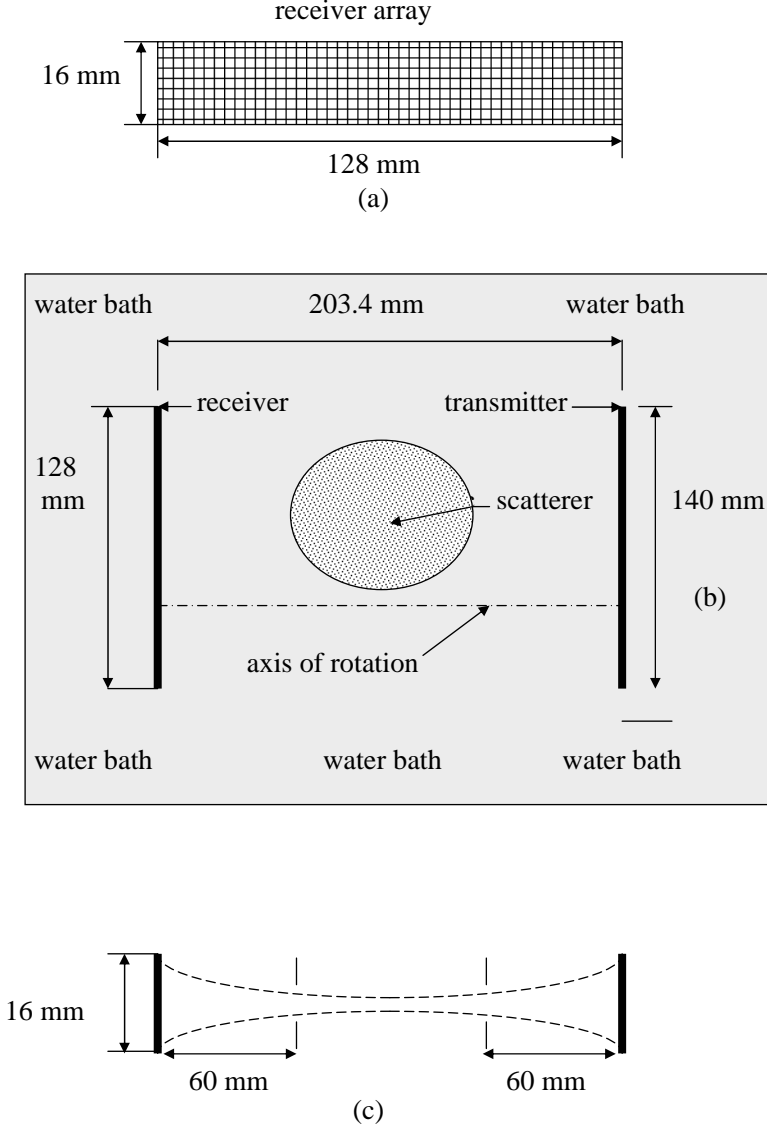


Figure 1: Figure 1. The geometry of the ultrasound scanner for acquiring ultrasonically scattered data in time and frequency. (a) The receiver array: 128 mm  $\times$  16 mm, 960 total elements. (b) The plan view of the scanner showing the scatterer and the transmitting-receiving arrangement. The entire set up is immersed in a water bath. The transmitter and receiver rotate as a solid body around the axis shown. Data collection is at every  $2^\circ$  of rotation. (c) The focusing geometry. Both the transmitter and the receiver are focused with a focal length of 60 mm. The transmitter has a lens for focusing while the receiver is surface is curved.

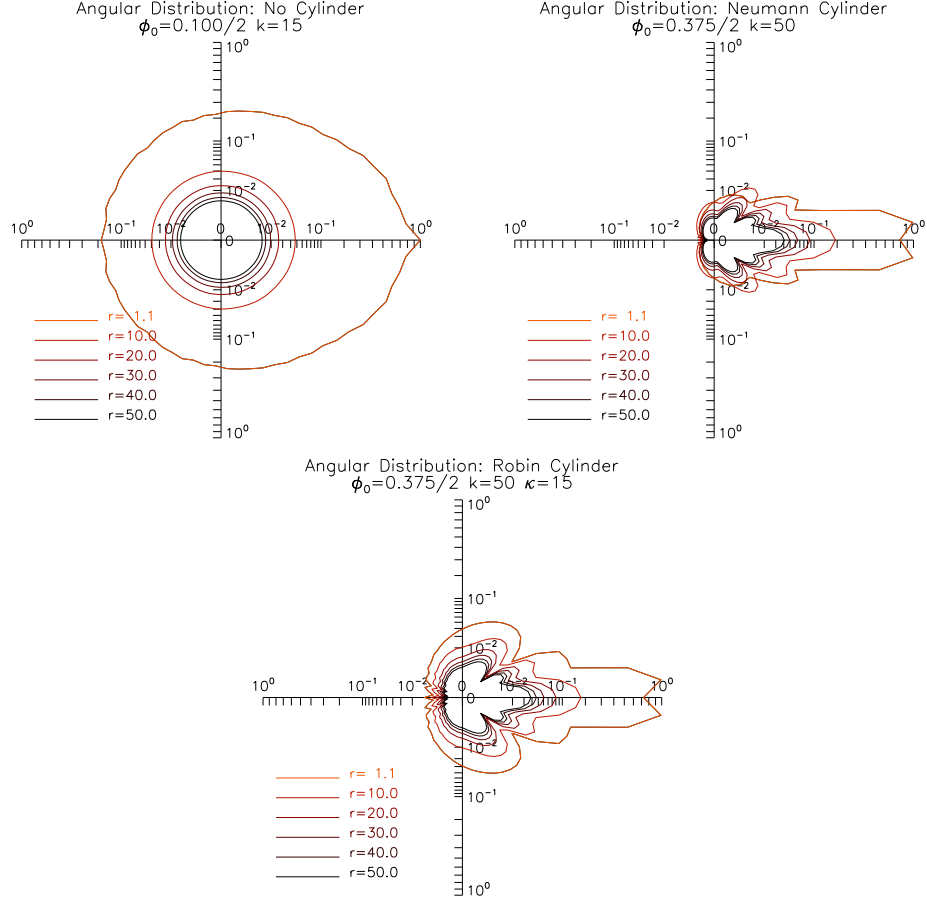


Figure 2: Plots showing the angular variation of the field emitted by a catheter-based miniature emitter. (a) A Neumann catheter.  $k_0 = 50$ , and  $\phi_0 = 0.185^\circ$ . (b) A Robin catheter.  $\alpha = 15$ .  $k_0$ ,  $\phi_0$  as in (a). (c) Emitter radiating in an unbounded space. Other parameters same as in (a).

# Noise propagation in linear and nonlinear inverse scattering

Dilip N. Ghosh Roy, John Roberts, and Matthias Schabel<sup>a)</sup>

Utah Center for Advanced Imaging Research, University of Utah, 729 Arapleen Drive, Salt Lake City, Utah 84108

Stephen J. Norton

Fitzpatrick Institute for Photonics, Duke University, Durham, North Carolina 27708

(Received 8 June 2006; revised 5 February 2007; accepted 6 February 2007)

The propagation of noise from the data to the reconstructed speed of sound image by inverse scattering within the framework of the Lippmann-Schwinger integral equation of scattering is discussed. The inversion algorithm that was used consisted in minimizing a Tikhonov functional in the unknown speed of sound. The gradient of the objective functional was computed by the method of the adjoint fields. An analytical expression for the inverse scattering covariance matrix of the image noise was derived. It was shown that the covariance matrix in the linear x-ray computed tomography is a special case of the inverse scattering matrix derived in this paper. The matrix was also analyzed in the limit of the linearized Born approximation, and the results were found to be in qualitative agreement with those recently reported in the literature for Born inversion using filtered backpropagation algorithm. Finally, the applicability of the analysis reported here to the obstacle problem and the physical optics approximation was discussed. © 2007 Acoustical Society of America. [DOI: 10.1121/1.2713671]

PACS number(s): 43.60.Pt, 43.60.Rw [EJS]

Pages: 2743–2749

## I. INTRODUCTION

Inverse scattering<sup>1–4</sup> is an intensely researched area in current applied mathematics, and has wide applications in almost all branches of modern science and technology, from medical imaging and nondestructive evaluation of materials to problems in astronomy. The general objective is to recover an unknown physical object (scatterer and/or inhomogeneity) from a set of appropriately defined data. The data in inverse scattering consist of fields scattered by the unknown object under wave excitation. The framework of analysis in this work is the famous *Lippmann-Schwinger* integral equation of scattering.<sup>1–4</sup> Let  $T$  denote the integral operator of scattering. If the scatterer is “weak,” then the uniform norm of  $T$ ,  $\|T\|_\infty \ll 1$ , where  $\|T\|_\infty = (1/2)(k_0 a)^2 \|1 - n\|_\infty$ .  $1 - n$  is the deviation of the scatterer refractive index  $n$  relative to that of the background which was assumed to be unity,  $k_0 = 2\pi/\lambda$  is the wave number of the exciting wave which is of wavelength  $\lambda$ .  $a$  is the dimension of the scatterer. Moreover,  $\|x(t)\|_\infty = \max |x(t)|$  over a certain interval of  $t$  and  $x$  in a suitable space  $X$ . In this case, the inverse scattering problem can be linearized by considering only the single scattering events. This is the well-known *Born* and *Rytov* approximation.<sup>5–7</sup> In these approximations, the incident wave is assumed to undergo a phase shift of less than  $\pi$  in traversing the scatterer. In general, however, the scatterer cannot be assumed to be weak. Also, in practice, scattering is frequently in the *resonance region* in which the wavelength is less than or comparable to the characteristic size of the scatterer.<sup>1</sup> Under such conditions,  $\|T\|_\infty$  cannot be considered to be small, and inverse problems in the resonance region are improperly posed

and nonlinear. The multiple scattering interactions between the propagating wave and the inhomogeneity must be taken into account. Linearization is, therefore, not possible, and the inverse solutions are usually obtained by iteratively minimizing a suitably constructed, regularized objective function.

The scattered fields measured at the detectors are always corrupted by noise, the sources of which are physical, but can also arise from the numerics. The reconstructed image is, therefore, also noisy. Moreover, the propagation of noise depends upon the mathematical procedure by which the data are transformed into the image, that is, the reconstruction algorithm. Thus the understanding of how noise in the data propagates to the image via a given reconstruction algorithm is clearly an important problem, not only for understanding the characteristics of the noise in the reconstructed images produced by the algorithm, but also for comparing the performances of reconstruction algorithms for given noise characteristics in the measurements. The propagation of noise under the weak scattering condition, where the linearized Born or Rytov approximation holds, has been investigated by several researchers.<sup>8–11</sup> In this paper, the attention is focused on the nonlinear inverse scattering of an arbitrary scatterer with frequencies in the resonance region.

The paper is organized as follows. The direct problem and its Fréchet differentiability are briefly reviewed in Sec. II. The inversion algorithm and the calculation of the gradient of a nonlinear functional via the *adjoint field*<sup>12–14</sup> are presented in Sec. III. The inverse scattering covariance matrix of the image noise is derived in Sec. IV, and its relation to that of the linear x-ray computed tomography appears in Sec. V. In Sec. VI, the inverse scattering covariance matrix is specialized to the limiting case of the Born approximation. Section VI also includes a short discussion about the applicability of the present analysis to obstacle problems and

<sup>a)</sup> Authors may be contacted at: <http://www.ucair.med.utah.edu>

physical optics approximation. Finally, a brief summary of the work is presented in Sec. VII.

## II. THE DIRECT PROBLEM AND FRÉCHET DIFFERENTIABILITY

The scattering is described by the *Lippmann-Schwinger* integral equation,<sup>1-4</sup> which is

$$\psi(x) = \psi^{\text{in}}(x) - k_0^2 \int_{\Omega} G^{(0)}(x|y) \gamma(y) \psi(y), \quad \Omega \in \mathbb{R}^d, \quad (1)$$

$$d = 2, 3,$$

subject to Sommerfeld's *radiation condition*:

$$\lim_{|x| \rightarrow \infty} |x|^m [\partial_{|x|} \psi^{\text{sc}} - ik_0 \psi^{\text{sc}}] = 0,$$

$m = (d-1)/2$ , and the limit is uniform in  $|x|$  in all directions, where  $d$  is the dimensionality of the problem.  $\Omega$  is the compact support of  $\gamma$ , that is, a bounded region in space.  $\psi^{\text{in}}(x) = e^{ik_0 x \cdot \hat{k}_0}$ ,  $\hat{k}_0 \in S^{d-1}$ , the unit sphere in  $\mathbb{R}^d$ , is the incident plane wave.  $\psi = \psi^{\text{in}} + \psi^{\text{sc}}$  is the *total field*,  $\psi^{\text{sc}}$  being the scattered component. From Eq. (1).

$$\psi^{\text{sc}}(x) = -k_0^2 \int_{\Omega} G^{(0)}(x|y) \gamma(y) \psi(y), \quad x \notin \Omega. \quad (2)$$

In Eqs. (1) and (2),  $\gamma(x) = 1 - (c_0/c(x))^2$  describes the spatial variation of the unknown inhomogeneity to be recovered, and the support of  $\gamma$  is assumed to be compact.  $c(x)$  is the speed of sound in the object.  $G^{(0)}(x|y)$  is the continuous free-space Green's function.  $G^{(0)}(x|y) = (i/4)H_0^{(1)}(k_0|x-y|)$  in two dimensions (2D), and  $G^{(0)}(x|y) = (1/4\pi)e^{ik_0|x-y|}/(|x-y|)$  in three dimensions.  $H_0^{(1)}$  is the zeroth-order Hankel function.<sup>15</sup>

The solution of Eq. (1) can be written as

$$\psi = \mathcal{L}^{-1} \psi^{\text{in}}. \quad (3)$$

In Eq. (3),  $\mathcal{L} = I + \mathcal{G}\gamma$ :  $L_2(\Omega) \rightarrow L_2(\Omega)$  is the Lippmann-Schwinger operator.  $I$  is the identity, and  $\mathcal{G}$  the Green function operator. Furthermore, Eq. (2) can be recast as

$$F(\gamma) = \psi^{\text{sc}}. \quad (4)$$

The scattering operator  $F(\gamma)$  in Eq. (4) is Fréchet differentiable. That is, there exists a linear operator,  $F'$ , the Fréchet derivative of  $F$ , such that  $\|F(\gamma+h) - F(\gamma) - F'h\| \sim o(\|h\|)$ ,  $h \in L_2(\Omega)$  being an arbitrary vector. Some details about the existence and uniqueness of the Fréchet derivative can be found in Hohage.<sup>16</sup>

The mathematical form of the derivative is of importance to the discussions that follow. A terse derivation is, therefore, presented. Let  $\tilde{\psi} = \gamma\psi$ . Then  $F(\gamma) = \mathcal{G}\tilde{\psi}$ , and Eq. (1) becomes

$$\mathcal{L}^{\dagger} \tilde{\psi} = \gamma \psi^{\text{in}}, \quad (5)$$

in which  $\mathcal{L}^{\dagger} = I - \gamma\mathcal{G}$  is the operator adjoint to  $\mathcal{L}$ . Also,

$$\psi = \psi^{\text{in}} + \mathcal{G}\tilde{\psi}, \quad (6)$$

Differentiating  $F(\gamma) = \mathcal{G}\tilde{\psi}$  formally in  $\gamma$  yields:  $F' = \mathcal{G}\tilde{\psi}'$ . From Eqs. (5) and (6), it is not difficult to show that  $\mathcal{L}^{\dagger}(\tilde{\psi}'h) = \psi'h$ , from which it follows that  $F' = \mathcal{G}[\mathcal{L}^{\dagger}]^{-1}\psi$ .

In finite space dimensions, the operators  $\mathcal{G}$ ,  $\mathcal{L}$ , and  $\mathcal{L}^{\dagger}$  are replaced by their corresponding matrix operators, which are denoted here by  $G$ ,  $L$ , and  $L^{\dagger}$ , respectively. We then obtain the Jacobian matrix of the scattered field, namely

$$J_{\text{sc}} = G[L^{\dagger}]^{-1}\Lambda_{\psi}, \quad (7)$$

and its transpose

$$J_{\text{sc}}^T = \Lambda_{\psi} L^{-1} G. \quad (8)$$

$\Lambda$  is used to denote a diagonal matrix. Thus  $\{\Lambda_{\psi}\}_{ij} = \psi_{ij}\delta_{ij}$ . Let  $M$  be the number of the detectors, and the grid be of size  $N \times N$ . Then  $J_{\text{sc}}$  is a  $M \times N^2$  matrix.

## III. THE INVERSION ALGORITHM

The solution of the inverse scattering problem was obtained by minimizing the following nonquadratic, Tikhonov type functional:

$$\Phi(\gamma) = (1/2)(\psi^{\text{sc}} - \psi^{\text{me}})^T \Sigma^{-1}(\psi^{\text{sc}} - \psi^{\text{me}}) + \alpha \|\gamma - \gamma^*\|_2^2. \quad (9)$$

$\psi^{\text{me}}$  is the measured (noisy) field,  $\Sigma$  the covariance matrix of the noisy measurements, and  $\alpha > 0$ ,  $\alpha$  small, the *regularization parameter*.  $\gamma^*$  is the initial estimate. It is known<sup>17</sup> that the regularizing term, as written in Eq. (9), contributes to the smoothness of the solution. It is to be noted that the functional,  $\Phi(\gamma)$ , is nonquadratic since the scattering operator,  $F(\gamma)$  in Eq. (4) is nonlinear.

Let  $\Phi_{,\gamma} = \nabla_{\gamma} \Phi$  be the functional derivative of  $\Phi$  with respect to  $\gamma$ . The basic reconstruction is then given by the solution which is the null point of the gradient. However, in order to calculate the error propagation from data to image, it is necessary to specify the mathematical form of the functional derivative. In the present work, the derivative was obtained via the use of the adjoint fields. The result is<sup>12</sup>

$$\Phi_{,\gamma} = \text{Re} \sum_{j=1}^{N_W} [\Lambda_{\psi_j} \psi_j^{\dagger}] + 2\alpha(\gamma - \gamma^*), \quad (10)$$

where  $N_W$  is the total number of the waves incident on the scatterer, and  $\psi_j^{\dagger}$  is the *adjoint field*.  $\psi_j^{\dagger}$  is given by

$$\psi_j^{\dagger} = L^{-1} \psi_j^{\dagger \text{in}}, \quad \psi_j^{\dagger \text{in}} = G \bar{r}_j. \quad (11)$$

In Eq. (11),  $\bar{r}_j = \psi_j^{\text{sc}} - \psi_j^{\text{me}}$  is the complex residual vector at the detectors. Its  $m$ th component,  $\psi_{jm}^{\text{sc}} - \psi_{jm}^{\text{me}}$ , the complex residual at the  $m$ th detector, is

$$\bar{r}_{jm} = [\text{Re}(r_{jm})/\text{Re}(\sigma_{jm}^2)] + i[\text{Im}(r_{jm})/\text{Im}(\sigma_{jm}^2)]. \quad (12)$$

$\text{Re}(\text{Im})$  is the real (imaginary) part of a complex variable, and the overbar implies complex conjugation.

A comparison of Eq. (11) with the Lippmann-Schwinger solution in Eq. (3) shows that  $\psi_j^{\dagger}$  can be obtained from Eq. (1) if  $\psi_j^{\dagger \text{in}}$  is substituted for  $\psi^{\text{in}}$  in that equation. Then from Eq. (10) it follows that the computation of the functional

derivative,  $\Phi_{,\gamma}$ , of the objective function,  $\Phi$  in Eq. (9), requires the solutions of only two forward problems, one for  $\psi$ , and another for  $\psi^\dagger$ , for any incidence. It should be mentioned at this point that a closely related problem occurs in nonlinear tomography where the derivative of a nonlinear operator is calculated via the solution of a linear adjoint problem, called *adjoint differentiation*.<sup>18</sup>

The reconstruction algorithm, therefore, consists in solving the system:  $\Phi_{,\gamma}=0$ . The solution of the inverse problem then reduces to that of locating the zeros of a nonlinear system of equations given in Eq. (10). It is this algorithm that forms the basis for the analysis of the image noise in this work.

#### IV. THE PROPAGATION OF NOISE

Let  $\xi=\langle\xi\rangle+\epsilon^\xi$  be a random quantity in which  $\langle\xi\rangle$  is the ensemble mean and  $\epsilon^\xi$  the noise component. Following this notation,  $\gamma=\langle\gamma\rangle+\epsilon^\gamma$ ,  $\psi=\langle\psi\rangle+\epsilon^\psi$ ,  $\psi^{\text{sc}}=\langle\psi^{\text{sc}}\rangle+\epsilon^{\text{sc}}$ ,  $\psi^\dagger=\langle\psi^\dagger\rangle+\epsilon^\dagger$ , and  $\psi^{\text{me}}=\langle\psi^{\text{me}}\rangle+n$ .  $\langle\psi^{\text{me}}\rangle$  is the noise-free data, and hence  $\langle\psi^{\text{me}}\rangle=\psi_{\text{tr}}^{\text{sc}}$ ,  $\psi_{\text{tr}}^{\text{sc}}$  denoting the field scattered by the true object. Implicit is the assumption that the magnitudes of the fluctuations are small compared to their mean values. Equation (10) now becomes

$$\begin{aligned}\Phi_{,\gamma} = & \text{Re}[\langle\psi\rangle\langle\psi^\dagger\rangle + \langle\psi\rangle\epsilon^\dagger + \langle\psi^\dagger\rangle\epsilon^\psi] \\ & + [\text{higher order terms}] + 2\alpha(\langle\gamma\rangle - \gamma^*) + 2\alpha\epsilon^\gamma.\end{aligned}\quad (13)$$

For the simplicity of notation, the sums over the index  $j$  for the incident field were omitted in Eq. (13). These will be introduced at the end. Setting the right-hand side of Eq. (13) to zero, and separating the mean and the random part, yields

$$\text{Re}[\langle\psi\rangle\langle\psi^\dagger\rangle] + 2\alpha(\langle\gamma\rangle - \gamma^*) = 0,$$

for the ensemble mean, and

$$\text{Re}[\langle\psi\rangle\epsilon^\dagger + \langle\psi^\dagger\rangle\epsilon^\psi] + 2\alpha\epsilon^\gamma = 0 \quad (14)$$

for the random part. We also introduce the assumption that the iterations have converged to within a  $\delta$  neighborhood of the solution, in which case, the term  $\langle\psi^\dagger\rangle\epsilon^\psi$  in Eq. (14) can be neglected, being of the higher order. Equation (14) then reduces to

$$\text{Re}[\Lambda_{\langle\psi\rangle}\epsilon^\dagger] + 2\alpha\Lambda_\gamma = 0, \quad (15)$$

where  $\Lambda$ , as earlier, denotes a diagonal matrix.

Noting that  $\langle\psi^\dagger\rangle \sim 0$  by virtue of the above-introduced assumption, the random part,  $\epsilon^\dagger$ , of the adjoint field,  $\psi^\dagger$ , is given by the relation:  $\epsilon^\dagger = \langle L \rangle^{-1} \epsilon^{\dagger\text{in}}$ , where  $\epsilon^{\dagger\text{in}}$  is the random part of  $\psi^{\dagger\text{in}} = G\bar{r}$ , as defined in Eq. (11). Moreover,  $\langle L \rangle$  is the Lippmann-Schwinger operator in which  $\gamma = \langle \gamma \rangle$ , i.e.,  $\langle L \rangle = I - G\Lambda_{\langle \gamma \rangle}$ . The quantity,  $\bar{r}$ , defined in Eq. (12), contains both the data noise,  $\bar{n}$ , as well as the noisy component of the scattered field. Let  $\bar{r}$  be written as:  $\bar{r} = \bar{r}^{\text{sc}} + \bar{n}$ , where  $\bar{r}^{\text{sc}}$  denotes the latter. Then

$$\epsilon^\dagger = \langle L \rangle^{-1} G[\bar{r}^{\text{sc}} + \bar{n}], \quad (16)$$

where  $\bar{r}^{\text{sc}}$  is the noise component of the scattered part of  $\bar{r}$  and  $n$  is the data noise. From the definition in Eq. (12) for  $\bar{r}$ :

$$\bar{r}_{jm}^{\text{sc}} = \frac{\text{Re } \bar{\epsilon}_{jm}^{\text{sc}}}{\text{Re } \sigma_{jm}^2} - i \frac{\text{Im } \bar{\epsilon}_{jm}^{\text{sc}}}{\text{Im } \sigma_{jm}^2}, \quad (17)$$

and a similar expression applies to  $\bar{n}$ . From Eqs. (8) and (16), one obtains

$$\text{Re}[\Lambda_{\langle\psi\rangle}\epsilon^\dagger] = \text{Re}[J_{\text{sc}}^T(\bar{r}^{\text{sc}} + \bar{n})]. \quad (18)$$

In order to proceed further, the scattered  $\epsilon^{\text{sc}}$  is expressed in terms of the object  $\epsilon^\gamma$ . It is readily verified that  $\epsilon^{\text{sc}} = J_{\text{sc}}\epsilon^\gamma$ . In view of Eq. (2),

$$\epsilon^{\text{sc}} = G\langle\gamma\rangle\epsilon^\psi. \quad (19)$$

Now replacing  $\gamma = \langle\gamma\rangle + \epsilon^\gamma$  and  $\psi = \langle\psi\rangle + \epsilon^\psi$  in the Lippmann-Schwinger Eq. (1), separating out the ensemble averaged and the random part on both sides of the result, it is readily obtained that

$$\epsilon^\psi = [\langle L \rangle^{-1} G\Lambda_{\langle\psi\rangle}]\epsilon^\gamma \quad (20)$$

to the first order. Substituting Eq. (20) in Eq. (19) then yields  $\epsilon^{\text{sc}} = J_{\text{sc}}\epsilon^\gamma$ , upon using Eq. (7). The identity also follows from the definition of the Jacobian matrix.

We next use the relation  $\epsilon^{\text{sc}} = J_{\text{sc}}\epsilon^\gamma$ , in Eq. (17), and replace the result in Eq. (18). Substituting the outcome in Eq. (15), and upon setting the result to zero yields

$$\begin{aligned}(\text{Re}(J_{\text{sc}}^T)\text{Re}(\Sigma^{-2})\text{Re}(J_{\text{sc}}) + \text{Im}(J_{\text{sc}}^T)\text{Im}(\Sigma^{-2})\text{Im}(J_{\text{sc}}) \\ + 2\alpha I)\epsilon^\gamma = \text{Re}(J_{\text{sc}}^T)\text{Re}(\Sigma^{-2})\text{Re}(\bar{n}) \\ + \text{Im}(J_{\text{sc}}^T)\text{Im}(\Sigma^{-2})\text{Im}(\bar{n}).\end{aligned}\quad (21)$$

In Eq. (21),  $\Sigma$  denotes the covariance matrix of the data noise. Thus  $\Sigma_{ij} = \sigma_{ij}$ .

In order to simplify the notations, let us define  $P_i[J] = P_i[\{\Sigma^{-1}\}[J_{\text{sc}}]]$ , and  $P_i[J^T] = P_i[\{J_{\text{sc}}^T\}P_i[\Sigma^{-1}]]$ ,  $i=1,2$ . The subscripts on  $P$  are used to indicate the real and imaginary parts of the operator. Thus  $P_{i=1}(P_{i=2})$  imply that only the real (imaginary) parts of the operators in the argument of  $P$  are to be considered. Moreover, we now sum over the number of incident waves  $N_W$  in the above-presented expressions, and define  $A = \sum_{j=1}^{N_W} \sum_{i=1}^2 P_i[J_j^T]P_i[J_j]$ , and  $B = \sum_{j=1}^{N_W} \sum_{i=1}^2 P_i[J_j^T]P_i[\bar{n}_j]$ . Equation (21) then takes the form:  $[A + 2\alpha I]\epsilon^\gamma = B\bar{n}$ , from which

$$\epsilon^\gamma = [A + 2\alpha I]^{-1} B\bar{n}. \quad (22)$$

Now  $\text{cov}(\gamma) = \langle \epsilon^\gamma \{ \epsilon^\gamma \}^T \rangle$ . From Eq. (22), it follows immediately that

$$\text{cov}(\gamma) = [A + 2\alpha I]^{-1} \langle B\bar{n} \{ B\bar{n} \}^T \rangle [A + 2\alpha I]^{-1}. \quad (23)$$

For a nonstochastic scatterer such as an acoustic inhomogeneity, it is reasonable to assume that data are uncorrelated with respect to the receiving transducers and view angles. The scattering data are, however, complex, and their real and imaginary parts are both corrupted by noise. This is

expressed through the complex  $\sigma$ . A correlation can exist between  $\sigma_{Re}$  and  $\sigma_{Im}$ . However, for a nonrandom acoustical scatterer, it is reasonable to neglect this correlation (see also Ref. 11). In other words,  $\text{cov}(n_{jm}, n_{j'm'}) = \sigma^2 \delta_{jj'} \delta_{mm'}$ . The covariance matrix in Eq. (23) then reduces to

$$\text{cov}(\gamma) = [A + 2\alpha I]^{-1} A [[A + 2\alpha I]^{-1}]^T. \quad (24)$$

Equation (24) is the covariance matrix of the image noise in the inverse scattering algorithm given in Eq. (10).

## V. LINEAR PROBLEM AND REAL DATA: X-RAY CT

The  $P$  operators in Sec. IV are nonlinear, i.e., they depend nonlinearly on the solution  $\langle \gamma \rangle$ . This is explicitly indicated in the fundamental equation of scattering, namely,  $\psi^{sc} = F(\gamma)$ , [Eq. (4), Sec. II].  $F(\gamma)$  indicates that  $F$  is a nonlinear functional of  $\gamma$ . Contrarily, if the operator  $F$  acts linearly on  $\gamma$ , as for example, if  $F$  is a matrix acting on a vector  $\gamma$ , then it is written as  $F_\gamma$ . In Eqs. (7) and (8) for the Jacobians, the nonlinearity is expressed through  $\Lambda_{\langle \psi \rangle}$  and  $\langle L \rangle$ , both of which are  $\langle \gamma \rangle$ -dependent. The complex nature of the scattered data introduces a further layer of complication. Clearly, the covariance matrix must simplify if the operator is linear and the data  $g$  are real, that is,  $g = F_\gamma$  instead of  $g = F(\gamma)$  as in Eq. (4).

An important case of a linear problem with real data is that of the x-ray computed tomography.<sup>19,20</sup> In x-ray CT, the scattering matrix  $F$  becomes the projection matrix  $H$ , the  $ij$ th element of which represents the intersection of the  $j$ th x ray with the  $i$ th resolution element. The noisy x-ray CT data can be written as  $g = H\gamma + n = \langle g \rangle + n$ . In this case, Eq. (24) for  $\text{cov}(\gamma)$  simplifies to

$$\text{cov}(\gamma) = [H^T \Sigma^{-2} H + 2\alpha]^{-1} [H^T \Sigma^{-2} H] \times [[H^T \Sigma^{-2} H + 2\alpha]^{-1}]^T. \quad (25)$$

A special case of Eq. (25) is the so-called MAP (*maximum a posteriori*) x-ray CT reconstruction algorithm<sup>21</sup> in maximum entropy with Poisson noise in the data. The corresponding objective function is given by

$$\Phi(\gamma) = \log\{p(g|\gamma)\} + \alpha \mathcal{R}(\gamma), \quad (26)$$

where  $\mathcal{R}(\gamma)$  is a positive definite symmetric matrix regularizer.  $p(g|\gamma)$  is the likelihood of data  $g$  given a distribution  $\gamma$ , assumed to be positive. For Poisson noise,

$$p(g|\gamma) = \prod_{j=1}^{MN} \left[ \exp\left(\sum_{i=1}^N H_{ji} \gamma_i\right) \frac{(\sum_{i=1}^N H_{ji} \gamma_i)^{g_j}}{g_j!} \right]. \quad (27)$$

Note that the quantity,  $g_j$ , in the denominator in Eq. (27) is an integer number, being the number of counts.  $MN$  is the total number of data,  $N$  being the size of the computational domain, and  $M$  the number of view angles. Carrying out the calculations of  $\Phi_{,\gamma}$  with the *log-likelihood function*,  $\log p(g|\gamma)$ ,  $p(g|\gamma)$  in Eq. (27), (for details, see Ref. 22), it is obtained that

$$[H^T \Sigma^{-2} H + \alpha^2 R] \epsilon^\gamma = H^T \Sigma^{-2} n. \quad (28)$$

From Eq. (28), the covariance for x-ray CT follows immediately. It is to be noted that for Poisson noise,  $\Sigma$  is the same as  $\Lambda_{\langle g \rangle}$ .

A comparison of Eqs. (24) and (28) shows that the error,  $\epsilon^\gamma$ , has the same mathematical form in both x-ray CT and acoustic inverse scattering, namely,

$$\epsilon^\gamma = [C + R(\alpha)]^{-1} E n,$$

where  $R(\alpha)$  is the regularizing term. However, in the case of linear x-ray CT,  $C$  and  $E$  involve the linear operator of projection,  $H$ , and its transpose. In acoustic inverse scattering, however,  $C$  and  $E$  are relatively more involved, being nonlinearly dependent in  $\gamma$ . Further details and an application of Eq. (28) to a dynamic SPECT problem appear in Ref. 22, and some related results can be found in Refs. 23–25.

## VI. THE LIMIT OF WEAK SCATTERING

In this section, Eq. (24) for the inverse scattering covariance matrix is analyzed in the limit of weak scattering in which the linearized Born approximation holds. Let us first assume that  $\text{Re } \sigma_{jm} = \text{Im } \sigma_{jm} = \sigma$ ,  $\forall j, m$ , and therefore,  $\text{Re } \Sigma^2 = \text{Im } \Sigma^2 = \sigma^2 I$ .  $\Sigma^2$  is a diagonal matrix:  $(\Sigma^2)_{ii} = \sigma_i^2$ . From now onward, attention will be confined to two dimensions.

Let

$$\mathcal{J} = \sum_{j=1}^{N_W} \text{Re}[J_j^T \bar{J}_j]. \quad (29)$$

In the Born approximation, Eq. (8) reduces to

$$J_j^T = {}^{\text{in}}\Lambda_j G. \quad (30)$$

${}^{\text{in}}\Lambda_j$  is the diagonal matrix for the  $j$ th incidence. That is,  $({}^{\text{in}}\Lambda_j)_{kk} = \exp(ik_0 \hat{d}_j \cdot x_k)$ ,  $\hat{d}_j$  being the unit vector specifying the direction of the  $j$ th incident wave. Also, the far-field Green's function has the form:

$$G_{k\ell} = \frac{e^{ik_0 R}}{\sqrt{R}} \left[ \frac{ia}{2} e^{-i\pi/4} \sqrt{\pi k_0} J_1(k_0 a) \right] e^{-ik_0 \hat{d}_\ell \cdot x_k}, \quad (31)$$

in which use was made of the asymptotic expression:<sup>1</sup>

$$H_n^{(1)}(t) = \sqrt{\frac{2}{\pi t}} e^{i(t-n\pi/2-\pi/4)} \left\{ 1 + \left( \frac{1}{t} \right) \right\}, \quad t \rightarrow \infty.$$

In Eq. (31),  $\hat{d}_\ell$  is the unit vector in the direction of the  $\ell$ th detector and  $R$  is the radius of the detector ring. The computational domain was assumed to have been discretized into  $N^2$  circular resolution elements following the widely used discretization scheme of Richmond.<sup>26</sup> The quantity,  $a$ , in Eq. (31), is the radius of such a circular pixel in the present, 2D, case. The geometry of the so discretized computational domain is shown in Fig. 1. In Fig. 1,  $x_k$  is the coordinate of the center of the  $k$ th circle in the grid, and  $\hat{d}_j$ ,  $\hat{d}_\ell$  are the unit vectors along the  $j$ th incident wave and the  $\ell$ th detector, respectively. The detectors are located on a ring of radius  $R$  surrounding the scatterer.

From Eqs. (30) and (31), we obtain the Jacobians in the Born approximation, namely



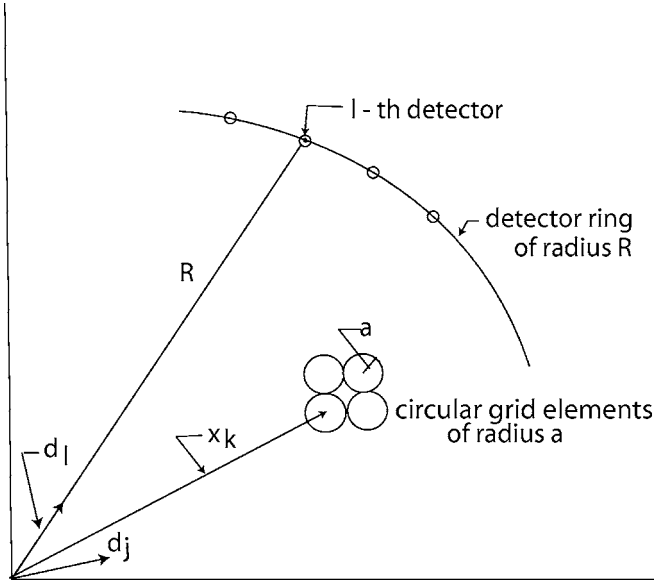


FIG. 1. A schematic of the geometry for the Born calculation illustrating the discretization of the computation grid into circular region.  $x_k$  is the location of the center of the  $k$ th resolution element in the grid.  $\hat{d}_j$ ,  $\hat{d}_\ell$  are the unit vectors along the  $j$ th incident wave and the  $\ell$ th detector, respectively. The detectors are located on a ring of radius  $R$  surrounding the scatterer. In the numerical computation in this work, the grid was discretized into  $32 \times 32$  circular elements each of radius  $a$ .  $R/a$  was 200. That is, the detectors were placed on a radius which was 200 times the radius of a circular pixel.

$$[J_j^T]_{km} = \frac{e^{ik_0 R}}{\sqrt{R}} \left[ \frac{ia}{2} e^{-i\pi/4} \sqrt{\pi k_0} J_1(k_0 \alpha) \right] e^{ik_0(\hat{d}_j - \hat{d}_m) \cdot x_k}, \quad (32)$$

and

$$[\bar{J}_j]_{m\ell} = \frac{e^{-ik_0 R}}{\sqrt{R}} \left[ -\frac{ia}{2} e^{i\pi/4} \sqrt{\pi k_0} J_1(k_0 \alpha) \right] e^{-ik_0(\hat{d}_j - \hat{d}_m) \cdot x_\ell}. \quad (33)$$

Replacing Eqs. (32) and (33) in Eq. (29), and after some straightforward algebra, it follows that

$$\mathcal{J}_{k\ell} = C \left[ \text{Re} \sum_{j=1}^{N_W} \sum_{m=1}^M e^{-ik_0(\hat{d}_j - \hat{d}_m) \cdot (x_k - x_\ell)} \right], \quad (34)$$

where the constant  $C = (\pi k_0 a^2 / 2R) [J_1(k_0 a)]^2$ . Note that Eq. (34) reflects the well-known fact that in the Born approximation the Fourier frequencies of the object are confined within a circle (in 2D) of radius  $2k_0$ , and therefore, the maximum frequency that can be present in the recovered object is bounded above by  $2k_0$ .

Typically in practice, the product  $N_W M$  is a large number for any realistic discretization of the computational domain. For example, for a  $64 \times 64$  size of the computational grid, this product is 4096 at the minimum. In practical computations, this number is often larger as the system is almost always overdetermined in actual numerics. We, therefore, approximate the sums in Eq. (34) by integrals. Moreover, the sums over  $j$  and  $m$  are independent sums. Assuming without any loss in generality that  $N_W = M$ , each individual sum can be approximated by

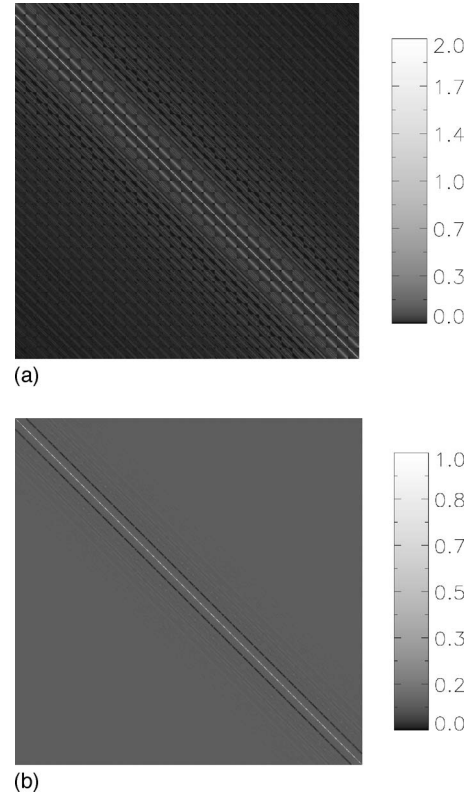


FIG. 2. (a) The  $1024 \times 1024$   $S$  matrix [Eq. (36)] for a  $32 \times 32$  grid. (b) The corresponding  $T$  matrix with  $\alpha = 10^{-4}$ . The block Toeplitz block structure of the matrices are visible.

$$\sum_{j=1}^{N_W} \cos(z \cos \phi) \sim \frac{N_W}{\pi} \int_0^\pi \cos(z \cos \phi) d\phi = N_W J_0(z), \quad (35)$$

recalling<sup>15</sup> that the integral in Eq. (35) is one of the representations of the cylindrical Bessel function  $J_0$ . Also, in Eq. (35),  $z = k_0 |x_k - x_\ell|$ .

In view of Eq. (35), Eq. (24) for the covariance reduces to the following expression in the Born approximation, namely

$$[\text{cov}^B(\gamma)] = \sigma^2 [T^{-1} S T^{-1}]. \quad (36)$$

In Eq. (36),  $S = C N_W^2 \mathcal{Z}$ ,  $\mathcal{Z}_{k\ell} = J_0^2(k_0 |x_k - x_\ell|)$ , and the constant  $C$  was defined earlier. Moreover,  $T = S + 2\alpha I$ . Note that  $S$  and  $T$  are each a block Toeplitz Toeplitz block or a BTTB matrix.<sup>27</sup>

It should be mentioned that the object enters the calculation through the noise in the data. In x-ray CT, for example, the object information is contained in  $\Sigma^{-2}$  in Eq. (28). Similarly, in the Born approximation, under the assumptions made in the derivation of Eq. (24) (essentially, the same assumptions also appear in Ref. 11), the object appears through  $\sigma^2$  in Eq. (36) which may originate, say, from speckles. Thus the behavior of the covariance is determined completely by Eq. (36). It is illustrated here assuming a  $32 \times 32$  computational grid.

The BTTB  $S$  matrix ( $1024 \times 1024$ ) is shown in Fig. 2(a), and the corresponding BTTB  $T$  matrix ( $1024 \times 1024$ ) is shown in Fig. 2(b) with the regularizing parameter  $\alpha = 10^{-4}$ .



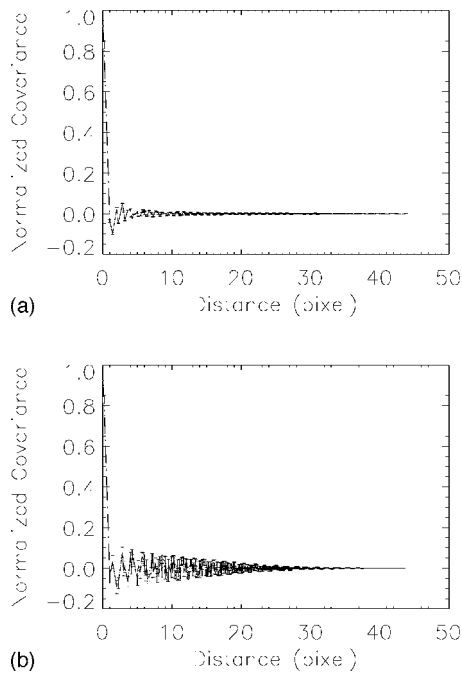


FIG. 3. The behavior of the covariance matrix,  $\text{cov}(\gamma)$  [Eq. (36)] with pixel separation. The variance or the diagonal elements of the matrix are constant. Panel (a) corresponds to the case in which  $\lambda/a=2$ , whereas (b) is for  $\lambda/a=3$ . Covariance is peaked at the center and falls off rapidly with the interpixel separation.

Toeplitz structures are clearly visible in Fig. 2. The covariance,  $\text{cov}^B(\gamma)$ , given in Eq. (36), is shown in Fig. 2. The variance is found to be constant in each pixel, whereas the off-diagonal elements of the covariance matrix are highly peaked around the center pixel, and decay rapidly in an oscillatory manner as the interpixel separation increases. In Fig. 3(a),  $\lambda/a$  was 2, while in Fig. 3(b),  $\lambda$  was three times the radius of a resolution element. In a recently published report,<sup>11</sup> the noise properties of Born objects were calculated using direct Born inversions. It is known<sup>5-7</sup> that Born data can be inferred by filtered backpropagation (FBPP), which is the analog of filtered backprojection of x-ray CT<sup>19,20</sup> in acoustical scattering. The behavior of the Born covariance matrix in Ref. 11 using FBPP inversion is qualitatively similar to that in Fig. 3. In both cases, the constant diagonal (the variance) and rapidly decaying oscillatory off-diagonal elements were obtained. Moreover, both methods produced  $\sigma^2$  dependence in the covariance matrix. However, the dependence on  $k_0$  is relatively more indirect in inverse scattering than in FBPP which produced a simple  $k_0^3$  dependence. Since the inversion algorithms are different, only a qualitative agreement is to be expected.

*Remark.* The preceding analysis of the propagation of noise from the data to the reconstructed image was carried out in the framework of the Lippmann-Schwinger integral equation of scattering. The Lippmann-Schwinger equation provides the appropriate framework for scattering calculations from inhomogeneities, that is, when the scattering potential has no discontinuity across its support. However, the analysis can also be extended to the obstacle problem in which the potential is discontinuous across its boundary. For the obstacle problem, the appropriate framework of analysis

is the *Helmholtz representation*,<sup>1,3</sup> which involves surface integrals. However, the inversion can be formulated into a problem in nonlinear parameter estimation<sup>1</sup> involving objective functions which are essentially similar to  $\Phi$  in Eq. (9). The parameters to be estimated in the case of the obstacles are the variables which parametrize the surface, e.g., spherical harmonics. The algorithm, Eq. (10), remains unchanged, and the functional derivative (now in the parametric variables of the surface) of the objective functional can again be obtained, as in the case of the inhomogeneities, via the method of adjoint fields, and again requiring the solutions of only two forward problems. The details of the procedure appear in Ref. 28. However, in the case of obstacle scattering, the derivatives are not the regular partial derivatives (as in Sec. III), but are the so-called *shape derivatives*,<sup>29-33</sup> which are defined in the following manner. If  $V: R^3 \rightarrow R^3$  is a vector field that deforms a domain  $\Omega_0 \in R^3 \rightarrow \Omega_t \in R^3$ ,  $t$  being the perturbation, then the first-order shape derivative of  $\psi$ ,  $\psi^{[1]}$ , is defined by

$$\psi^{[1]} = \lim_{t \rightarrow 0} \frac{\psi_t(I + tV)(X) - \psi_0(X)}{t}, \quad \forall X \in R^3.$$

$\psi_0$ ,  $\psi_t$  denote the fields for the unperturbed and perturbed boundary, respectively, corresponding to the boundary condition of the scattering problem,  $\psi^{[1]}$  is the *total, material, or substantial derivative*. Moreover,  $\psi^{[1]} = \psi' + V \cdot \nabla \phi$ ,  $\psi'$  being the partial derivative, namely,  $\psi' = \lim_{t \rightarrow 0} [\psi_t(X) - \psi_0(X)]/t$ .

In a similar vein, the analysis can also be extended to the limit of the physical optics approximation. It is to be noted that the physical optics approximation bears the same relation to the Helmholtz representation as the Born approximation does to the Lippmann-Schwinger integral equation. In both cases, the total field within the surface integrals is replaced by the incident waves weighted by suitable constants.

## VII. CONCLUSIONS

The propagation of noise from the data to the speed of sound image, reconstructed by inverse scattering within the framework of the Lippmann-Schwinger integral equation of scattering, was investigated. The inversion algorithm constituted in locating the zeros of the gradient of a Tikhonov-type functional in the unknown speed of sound. The gradient of the functional was computed by the method of the adjoint fields. An analytical expression was obtained for the image covariance matrix. When applied to the case of a linear mapping with real data, the inverse scattering expression reduced to that of the linear x-ray computed tomography. This was demonstrated by considering the maximum *a posteriori* likelihood algorithm using the maximum entropy functional. The full inverse scattering covariance was also investigated in the limiting case of the linearized Born approximation. It was found that in this linearized approximation, the variance remained uniform over the image, whereas the off-diagonal elements of the covariance matrix exhibited a fast decaying oscillatory behavior. Similar behaviors were also obtained in a recent report on Born inversion using the filtered backprojection algorithm. Finally, the applicability of the analysis presented to the problem of obstacle scattering and in the

limit of the physical optics approximation was briefly discussed.

## ACKNOWLEDGMENTS

This work was supported by a New Investigator Award, W81XWH-04-1-0042, under the Department of Defense Prostate Research Program.

- <sup>1</sup>D. Colton and R. Kress, *Inverse Acoustic and Electromagnetic Scattering Theory* (Springer, Berlin, 1992).
- <sup>2</sup>A. Kirsch, *An Introduction to the Mathematical Theory of Inverse Problems* (Springer, Berlin, 1986).
- <sup>3</sup>D. N. G. Roy and L. S. Couchman, *Inverse Problems and Inverse Scattering of Plane Waves* (Academic, London, 2002).
- <sup>4</sup>A. Ramm, *Multidimensional Inverse Problems* (Longman and Pitt, New York, 1992).
- <sup>5</sup>A. J. Devaney, "Diffraction tomography," in *Inverse Methods in Electromagnetic Imaging, Part 2*, edited by W. M. Boerner, NATO ASI Series (Reidel, 1983), pp. 1107–1135.
- <sup>6</sup>K. J. Langenberg, "Applied inverse problems for acoustic, electromagnetic and elastic wave scattering," in *Basic Methods of Tomography and Inverse Problems*, edited by P. C. Sabatier (Adam Hilger, Bristol, 1987).
- <sup>7</sup>A. C. Kak and M. Slaney, *Principles of Computerized Tomographic Imaging* (SIAM, Philadelphia, 2001).
- <sup>8</sup>D. Rouseff and R. Porter, "Diffraction tomography and stochastic inverse problem," *J. Acoust. Soc. Am.* **89**, 1599–1605 (1991).
- <sup>9</sup>G. Tsihrintzis and A. Devaney, "Application of a maximum likelihood estimator in the experimental study in ultrasonic diffraction tomography," *IEEE Trans. Med. Imaging* **12**, 545–554 (1993).
- <sup>10</sup>X. Pan, "A unified reconstruction theory for diffraction tomography with considerations of noise control," *J. Opt. Soc. Am. A* **15**, 2312–2326 (1998).
- <sup>11</sup>M. Anastasio, M. A. Kupinski, and X. Pan, "Noise propagation in diffraction tomography: Comparison of conventional algorithms with a new reconstruction algorithm," *IEEE Trans. Nucl. Sci.* **45**, 2216–2223 (1998).
- <sup>12</sup>S. J. Norton, "Iterative inverse scattering algorithms: Methods of computing Fréchet derivatives," *J. Acoust. Soc. Am.* **106**, 2653–2660 (1999).
- <sup>13</sup>O. Dorn, H. Bertete-Aguirre, J. G. Berryman, and G. C. Papanicolau, "A nonlinear inversion method for 3d electromagnetic imaging using adjoint fields," *Inverse Probl.* **15**, 1523–1558 (1999).
- <sup>14</sup>P. R. McGillivray and D. W. Oldenburg, "Methods for calculating Fréchet derivatives and sensitivities for the non-linear inverse problem: A comparative study," *Geophys. Prospect.* **38**, 499–524 (1994).
- <sup>15</sup>M. Abramowitz and I. Stegun, *Handbook of Mathematical Functions* (Dover, New York, 1972).
- <sup>16</sup>T. Hohage, "On the numerical solution of a three-dimensional inverse medium scattering problem," *Inverse Probl.* **17**, 1743–1763 (2001).
- <sup>17</sup>H. W. Engl, M. Hanke, and A. Neubauer, *Regularization of Ill-posed Problems* (Kluwer, Dordrecht, 1996).
- <sup>18</sup>F. Natterer and F. Wübbeling, *Mathematical Methods in Image Reconstruction* (SIAM, Philadelphia, 2001).
- <sup>19</sup>H. H. Barrett and W. Swindell, *Radiological Imaging: The Theory of Image Formation, Detection, and Processing* (Academic, New York, 1996).
- <sup>20</sup>F. Natterer, *The Mathematics of Computerized Tomography* (Teubner, Stuttgart, 1986).
- <sup>21</sup>S. M. Kay, *Fundamentals of Statistical Signal Processing* (Prentice Hall, Englewood Cliffs, NJ, 1998).
- <sup>22</sup>G. T. Gullberg, R. H. Huesman, D. N. G. Roy, J. Qi, and B. W. Reutter, "Estimation of the parameter covariance matrix for a one-compartment cardiac perfusion model estimated from a dynamic sequence reconstructed using map iterative reconstruction algorithms," in *IEEE Nuclear Science Symposium and Medical Imaging Conference Record*, Portland, Oregon, 2003, pp. 3019–3023.
- <sup>23</sup>H. H. Barrett, D. W. Wilson, and B. M. W. Tsu, "Noise properties of the em algorithm I. Theory," *Phys. Med. Biol.* **39**, 833–846 (1994).
- <sup>24</sup>J. Qi and R. M. Leahy, "Resolution and noise properties of map reconstruction for fully 3-D PET," *IEEE Trans. Med. Imaging* **19**, 493–506 (2000).
- <sup>25</sup>J. A. Fessler, "Mean and variance of implicitly defined biased estimators (such as penalized maximum likelihood): Applications to tomography," *IEEE Trans. Image Process.* **5**, 493–506 (1996).
- <sup>26</sup>J. H. Richmond, "Scattering by a dielectric cylinder of arbitrary cross section shape," *IEEE Trans. Antennas Propag.* **AP-13**, 334–341 (1965).
- <sup>27</sup>K. Chen, *Matrix Preconditioning Techniques and Applications* (Cambridge University Press, Cambridge, 2005).
- <sup>28</sup>S. J. Norton, "Iterative algorithms for computing the shape of a hard scattering object: Computing the shape derivative," *J. Acoust. Soc. Am.* **116**, 1002–1008 (2004).
- <sup>29</sup>O. Pironneau, *Optimal Shape Design for Elliptic Systems* (Springer, Berlin, 1984).
- <sup>30</sup>A. Zochowski, *Mathematical Problems in Shape Optimization and Shape Memory Materials* (Lang, New York, 1992).
- <sup>31</sup>O. Bruno and F. Reitich, "A new approach to the solution of problems of scattering by bounded obstacle," *Proc. SPIE* **122A**, 20–27 (1995).
- <sup>32</sup>D. N. G. Roy, L. Couchman, and J. Warner, "Scattering and inverse scattering of sound-hard obstacles via shape deformation," *Inverse Probl.* **13**, 585–606 (1997).
- <sup>33</sup>D. N. G. Roy, J. Warner, L. Couchman, and J. Shirron, "Inverse obstacle transmission problem in acoustics," *Inverse Probl.* **14**, 903–929 (1998).

# Acoustical Wave Propagation In a Cylindrical Waveguide In The Presence of Flow

D. N. Ghosh Roy<sup>\*</sup>, J. Roberts, and M. Schabel

*Utah Center for Advanced Imaging Research, University of Utah,  
729 Arapleen Dr., Salt Lake City, UT 84108, USA*

---

## Abstract

The propagation of acoustic waves in a circularly cylindrical waveguide in the presence of flow was investigated. An integral equation for the total pressure in the duct was derived, and subsequently reduced in the Born limit, i.e., for flow speeds much slower than the speed of sound in the quiescent medium. The Born term was then used to determine the mode phase speeds, and hence the effects of flow on wave propagation in the duct. Results are reported for the parabolic laminar and a mixed parabolic-flat turbulent velocity distribution of a homogeneous fluid flowing inside ducts of Dirichlet, Neumann and Robin surfaces. For the Neumann boundary and mixed flow, the integral equation yielded results similar to those obtained by recently reported perturbative calculations. However, the mathematics is more transparent in the integral equation method which is also more versatile, and can be applied with relative ease to numerous practical situations which may involve inhomogeneous media, arbitrary flow profiles and boundaries.

*Key words:*

*PACS:*

---

## 1 Introduction

The propagation of acoustic waves in circular ducts carrying flow is an important problem with a well-developed literature [1–13]. Various techniques exist for the solution of the problem including series solutions of the governing differential equations (e.g., [8, 10]), finite element calculations (e.g., [6, 12]), and hydrodynamical approach (see e.g., [9, 13]). Recently, a perturbative approach was reported [11] for calculating the changes in the mode phase speeds due to flow in a sound-hard duct with a view to obtaining accurate flow metering (see also [5] for this application). In this paper, we discuss the application of the integral equation approach, well-known [14, 15] from acoustical scattering theory, to the solution of the wave propagation problem in a duct in the presence of flow. A formal integral equation is derived for the total pressure field in the flowing fluid, which is then reduced in the Born limit. In this limit, it is assumed that the flow speeds are much slower than the speed of sound in the quiescent medium (ie. in the absence of flow). The method was used in order to determine the mode phase speeds in the presence of the flow, and hence investigate the effects of the flow on the wave propagation. Results were obtained for the laminar parabolic as well as a mixed laminar-turbulent velocity profile of the fluid flowing in ducts with a Dirichlet (sound-soft), Neumann (sound-hard) and Robin (impedance) boundaries.

In the Born approximation, with Neumann boundary, the integral equation produced results similar to those that were obtained in [11] using a perturbative approach. The mathematics of the present method is, however, more

---

\* Corresponding author.

*Email address:* `dilip@uclair.med.utah.edu` (D. N. Ghosh Roy).

transparent. Unlike most methods, the integral equation does not (*a priori*) assume any particular form of the pressure field except its time harmonicity. The field is rather a result of the calculations. In addition, the integral equation formalism is applicable to problems including nonuniform flow and arbitrary velocity profiles and boundary conditions. In addition, the powerful techniques that exist for solving various acoustical scattering and inverse scattering problems, can be brought to bear on the problem of flow under quite general conditions.

The plan of the presentation is as follows. In Section 2, the basic equations are presented, and a formal solution for the total pressure field in a flowing fluid is developed. The solution is then specialized to the Born limit. Section 3 derives Green's functions which satisfy the boundary condition and Sommerfeld's radiation condition at infinity. In Section 4, the incident pressure and the Born approximated total pressure field are derived. Section 4 further demonstrates how the Born approximated inhomogeneous part of the total pressure leads to the determinations of the phase speeds of the propagating modes in the presence of flow. Section 5 contains the details of the numerics. The results obtained are then discussed in the following Section 6. The text is concluded by a few remarks on the extension of the integral equation approach to general flow profiles, fluid media and waveguide surfaces.

## 2 The Equations of Wave Propagation

Consider the flow of a homogeneous fluid in a long cylinder of radius  $R$ . Let  $\mathbf{V} = \{v_i\}_{i=1}^3$  describe the velocity field of the fluid. Then  $t = t'$ ,  $x_i = x_i + v_i t'$  represent the coordinate transformations between the laboratory (unprimed)

system and the one co-moving with the flow (primed). In the primed coordinate system, the flow equations are:

$$\frac{\partial \rho}{\partial t'} + \rho_0 \sum_i \frac{\partial v_i}{\partial x'_i} = 0 : \text{momentum conservation}, \quad (1)$$

$$\rho_0 \frac{\partial v_i}{\partial t'} + \frac{\partial p}{\partial x'_i} = 0 : \text{mass conservation}, \quad (2)$$

$\rho$  and  $\rho_0$  are the perturbed and unperturbed mass density, respectively, and  $p$  is the pressure. It is well-known [16] that under the above coordinate transformation, Eqs. (1) and (2) combine to yield:

$$\nabla^2 p + k_0^2 \left[ 1 + \frac{i}{\omega} \mathbf{V} \cdot \nabla \right]^2 p = 0, \quad (3)$$

assuming time harmonicity.  $\omega$  is the angular frequency, and  $k_0 = \omega/c_0$  the wavenumber,  $c_0$  being the sound speed in the quiescent medium. In the first approximation with respect to the Mach number,  $\mathbf{M} = |\mathbf{V}_{\max}|/c_0$ , and assuming that the flow is quasi-steady (typical time variation  $\tau \gg \omega^{-1}$ ), the second-order term in Eq. (3) can be neglected [17] resulting in the approximation:

$$\nabla^2 p + k_0^2 \left[ 1 + \frac{2i}{\omega} \mathbf{V} \cdot \nabla \right] p = 0. \quad (4)$$

In cylindrical coordinates  $\mathbf{r} = \{\rho, \phi, z\}$ ,  $\nabla^2 = \nabla_{\perp}^2 + \rho^{-2} \partial_{\phi\phi} + \partial_{zz}$  with  $\nabla_{\perp}^2 = \partial_{\rho\rho} + (1/\rho) \partial_{\rho}$ . It is further assumed that the flow is along the  $z$ -direction which is also the directrix of the cylindrical waveguide and is radially varying. Therefore,  $\mathbf{V} = \mathbf{V}(\rho, \phi, z) = \hat{\mathbf{z}} V(\rho)$ ,  $\hat{\mathbf{z}}$  being the unit vector in the  $z$ -direction. Equation (4) then becomes:

$$\nabla^2 p + k_0^2 \left[ 1 + \frac{2i}{\omega} V(\rho) \right] \frac{\partial p}{\partial z} = 0. \quad (5)$$

Let  $G^{(0)}(\mathbf{r}|\mathbf{r}_S)$  be the “free-space” Green’s function, that is, Green’s function in the quiescent fluid, between the source location,  $\mathbf{r}_S$ , and the observation point  $\mathbf{r}$ . It is described by:

$$\left[\nabla^2 + k_0^2\right] G^{(0)}(\mathbf{r}|\mathbf{r}_S) = -\frac{1}{\rho}\delta(\rho - \rho_S)\delta(\phi - \phi_S)\delta(z - z_S). \quad (6)$$

Furthermore, let  $G^{(0)}(\mathbf{r}|\mathbf{r}_S)$  also satisfy the boundary condition on the waveguide, namely

$$\mathcal{B}G^{(0)} = 0 \text{ on the surface of the cylinder,} \quad (7)$$

$\mathcal{B}$  being the boundary operator.  $\mathcal{B} = \mathbf{I}$ ,  $\mathbf{I}$  the identity operator, corresponds to the Dirichlet,  $\mathcal{B} = \hat{\mathbf{n}} \cdot \nabla$ ,  $\hat{\mathbf{n}}$  the unit normal on the boundary, to the Neumann, and  $\mathcal{B} = \hat{\mathbf{n}} \cdot \nabla + i\alpha$  to the Robin boundary. The parameter  $\alpha$  denotes the quantity  $R\beta$ ,  $\beta = \beta' + i\beta''$  being the acoustic admittance of the cylinder wall. In terms of  $G^{(0)}$ , the total pressure,  $p$ , at any point in the fluid, can be obtained from Eq. (5) as:

$$p(\mathbf{r}) = p^{\text{inc}}(\mathbf{r}) + \int_{\Omega} d\mathbf{r}' \left\{ \tilde{V}(\mathbf{r}') G^{(0)}(\mathbf{r}|\mathbf{r}') \frac{\partial}{\partial z} \right\} p(\mathbf{r}'). \quad (8)$$

$p^{\text{inc}}(\mathbf{r})$  is an appropriate incident pressure field, and  $\Omega$  is the volume of the waveguide. Moreover, in Eq. (8),  $\tilde{V}(x) = -(2ik_0/c_0)V(x)$ .

Equation (8) is essentially the *Lippmann-Schwinger* integral equation of scattering [14, 15] except that the propagator is now  $G^{(0)}(\mathbf{r}|\mathbf{r}')\{\partial/\partial z\}$  instead of  $G^{(0)}$  alone, as in the usual scattering equation. It is noteworthy that the flow itself (via  $V(\mathbf{r})$ ) provides the scattering centers and acts as an inhomogeneity, no physical particulate matters being necessary to provide the centers, although the presence of additional physical inhomogeneities (of arbitrary nature) poses

no problem in the integral equation approach. In other words, the flow gives rise to what may be termed *acoustic velocity inhomogeneity* for diffraction (see also [18]). Since the diffraction scales as the Mach number [19], the scattering from the velocity inhomogeneity will indeed be small for  $\mathbf{M} \ll 1$ , and the *Born approximation* can be invoked. It is well-known [14–16, 20, 21] that in the Born approximation, Eq. (8) reduces to:

$$p(\mathbf{r}) = p^{\text{inc}}(\mathbf{r}) + \int_{\Omega} d\mathbf{r}' \left\{ \tilde{V}(\mathbf{r}') G^{(0)}(\mathbf{r}|\mathbf{r}') \frac{\partial}{\partial z} \right\} p^{\text{inc}}(\mathbf{r}'). \quad (9)$$

In other words, the Born approximation consists in replacing the total pressure,  $p$ , in the integral by the incident field,  $p^{\text{inc}}$ . The integral on the right-hand-side of Eq. (9) is the inhomogeneous term in the solution for the total pressure,  $p$ , and is denoted by  $p_{\text{ih}}$  in the sequel. Therefore,  $p(\mathbf{r}) = p^{\text{inc}}(\mathbf{r}) + p_{\text{ih}}(\mathbf{r})$ . It is Eq. (9) which is of interest here.

The free-space Green's function,  $G^{(0)}$ , is derived next.

### 3 The "Free-Space" Green's Function

As was already pointed out, unlike the standard Green's functions in an unbounded space ( $(i/4)H_0^{(1)}(k_0|x-y|)$ ) in 2-D,  $H_0^{(1)}$  being the cylindrical Hankel function of order zero of the first kind [22] and  $\exp(ik_0|x-y|)/4\pi|x-y|$  in 3D),  $G^{(0)}$  here is a *boundary Green's function* which satisfies both the condition on  $p$  imposed on the boundary of the waveguide, as well as the radiation condition at infinity. For a boundary of arbitrary shape, this Green's function may be difficult to obtain, but fortunately for boundaries of canonical shapes (as in the present case), it can be obtained rather easily.



In order to obtain an expression for  $G^{(0)}$ , we first note that:

$$\delta(\phi - \phi_S) = \frac{1}{2\pi} \sum_{\ell=-\infty}^{\infty} e^{i\ell(\phi - \phi_S)} \quad (10)$$

in terms of the definition of the angular Fourier transform pair,  $(f(\phi), \hat{f}(m))$  :

$$f(\phi) = \sum_{m=-\infty}^{\infty} \hat{f}(m) e^{im\phi}, \quad \hat{f}(m) = \frac{1}{2\pi} \int_{-\pi}^{\pi} f(\phi) e^{-im\phi} d\phi.$$

Moreover, upon using the orthogonality relation for the Bessel functions:

$$\int_0^R dr r J_n(\kappa_{\ell s} r) J_n(\kappa'_{\ell s} r) = 0, \quad \kappa_{\ell s} \neq \kappa'_{\ell s}, \quad (11)$$

which is known to hold under quite general conditions [23], the radial delta function,  $(1/\rho)\delta(\rho - \rho_S)$ , can be expressed as:

$$\frac{1}{\rho} \delta(\rho - \rho_S) = \frac{2}{R^2} \sum_L \tilde{J}_L(\rho) \tilde{J}_L(\rho_S), \quad (12)$$

$L$  in Eq. (12) denotes the joint indices,  $\{\ell s\}$ . In other words,  $\sum_L = \sum_{\ell=0}^{\infty} \sum_{s=0}^{\infty}$ .

The orthonormalized Bessel function,  $\tilde{J}_L(z)$ , is:

$$\tilde{J}_L(z) = A_L^{-1} J_{\ell} \left( \kappa_L \frac{z}{R} \right), \quad (13)$$

the normalization constant,  $A_L$ , being:

$$A_L = \frac{R}{\sqrt{2}} \left[ \int_0^R d\rho \rho \left[ J_{\ell}^2 \left( \kappa_L \frac{\rho}{R} \right) \right] \right]^{\frac{1}{2}}. \quad (14)$$

The eigenvalues,  $\kappa_L$ , in Eqs. (13) and (14), are obtained from the operator equation,

$$\mathcal{K}(\kappa_L) = 0, \quad (15)$$

the operator,  $\mathcal{K}$ , being boundary dependent via Eq. (7). From Eqs. (10), (12), and (6), it follows that:

$$\left[\nabla^2 + k_0^2\right] G^{(0)}(\mathbf{r}|\mathbf{r}_S) = -\frac{1}{\pi R^2} \sum_L e^{i\ell(\phi-\phi_S)} \tilde{g}_L(\rho, \rho_S) \delta(z - z_S; L), \quad (16)$$

where  $\tilde{g}_L(\rho, \rho_S) = \tilde{J}_L(\rho) \tilde{J}_L(\rho_S)$ .

Let

$$g_\ell(\rho, \rho_S; z, z_S) = \tilde{g}_L(\rho, \rho_S) \tilde{g}_L(z, z_S), \quad (17)$$

be the *reduced* Green's function. Equation (16) then becomes:

$$G^{(0)}(\mathbf{r}|\mathbf{r}_S) = -\frac{1}{\pi R^2} \sum_L e^{i\ell(\phi-\phi_S)} \tilde{g}_L(\rho, \rho_S) \tilde{g}_L(z, z_S). \quad (18)$$

From Eqs. (18) and (16), it is readily seen that  $\tilde{g}_L(z, z_S)$  is given by the equation:

$$\left\{\partial_{zz} + \Lambda_L^2\right\} \tilde{g}_L(z, z_S) = -\delta(z - z_S), \quad (19)$$

where  $\Lambda_L = \sqrt{k_0^2 - \left(\frac{\kappa_L}{R}\right)^2}$ . The solution of Eq. (19) is:

$$\tilde{g}_L(z, z_S) = \frac{i}{2} \frac{1}{\Lambda_L} e^{i\Lambda_L|z-z_S|}. \quad (20)$$

Collecting the results in Eqs. (17), (18), and (20), the free-space Green's function in the waveguide is finally derived to be:

$$G^{(0)}(\mathbf{r}|\mathbf{r}_S) = -\frac{i}{\pi R^2} \sum_L e^{i\ell(\phi-\phi_S)} \tilde{J}_L(\rho) \tilde{J}_L(\rho_S) \frac{1}{\Lambda_L} e^{i\Lambda_L|z-z_S|}. \quad (21)$$

The phase speed of the waves,  $c_L = \omega/\Lambda_L$ , is boundary dependent through  $\Lambda_L$ .

## 4 The Total Pressure

The total pressure,  $p$ , is given by Eq. (9). The incident pressure,  $p^{\text{inc}}$ , is given by:

$$p^{\text{inc}}(\mathbf{r}) = \sum_L p_L^{(0)} e^{i\ell\phi} J_L(\rho) e^{i\Lambda_L z} \quad (22)$$

corresponding to  $V = 0$ . Replacing Eqs. (21) and (23) in Eq. (9), and after some straightforward algebra, the total pressure,  $p$ , is obtained:

$$p(\mathbf{r}) = \sum_L p_L^{(0)} e^{i\ell\phi} J_L(\rho) e^{i\Lambda_L z} - \frac{i}{\pi R^2} \sum_L \sum_{s'} p_{L'}^{(0)} \frac{\Lambda_{L'}}{\Lambda_L} \mathcal{C}_{L,s'}(R) e^{i\ell\phi} \tilde{J}_L(\rho) \cdot \int_{R^1} dz' e^{i\Lambda_L |z-z'|} e^{i\Lambda_{L'} z'}. \quad (23)$$

In Eq. (23),  $L' = \{\ell, s'\}$ , and  $L, s' = \{\ell, s, s'\}$ . Moreover, the quantity,  $\mathcal{C}_{L,s'}(R)$  is given by:

$$\mathcal{C}_{L,s'}(R) = \frac{2k_0^2}{\omega} \int_0^R d\rho' \rho' \tilde{J}_L(\rho') V(\rho') J_{L'}(\rho').$$

Let us next define the quantity:

$$\mathcal{F}_{L,s'} = -\frac{2i}{R^2} p_{L'}^{(0)} \frac{e^{i\ell\phi}}{\Lambda_L} \tilde{J}_\ell \left( \kappa_L \frac{\rho}{R} \right) \int_{R^1} dz' e^{i\Lambda_L |z-z'|} e^{i\Lambda_{L'} z'}. \quad (24)$$

In view of Eq. (24), the inhomogeneous part of the solution,  $p_{\text{ih}}$  in Eq. (23) can be written as:

$$p_{\text{ih}}(\mathbf{r}) = \sum_L \sum_{s'} \Lambda_{Ls'} \mathcal{C}_{Ls'} \mathcal{F}_{Ls'}. \quad (25)$$

At this point, let us note that:

$$G^{(0)} * p^{\text{inc}} = \sum_L \sum_{s'} C_{L,s'}^{(0)} \mathcal{F}_{L,s'}, \quad (26)$$

in which

$$C_{L,s'}^{(0)} = \int_0^R d\rho \rho \tilde{J}_\ell \left( \frac{\kappa_L}{R} \rho \right) J_\ell \left( \frac{\kappa_{L'}}{R} \rho \right),$$

and  $*$  denotes the operation of convolution. Using Eq. (26) in Eq. (25) results in:

$$p_{\text{ih}}(\mathbf{r}) = \sum_L \sum_{s'} \Lambda_{L'} \frac{C_{L,s'}}{C_{L,s'}^{(0)}} \left( G^{(0)} * p^{\text{inc}} \right)_{L,s'}. \quad (27)$$

Since from the orthogonality relation (11),  $C_{L,,s'}^{(0)} = (R^2/2)A_{L,s'}^2\delta_{ss'}$ , Eq. (27) then becomes:

$$p_{\text{ih}}(\mathbf{r}) = \sum_L \Lambda_L \frac{C_L}{C_L^{(0)}} \left( G^{(0)} * p^{\text{inc}} \right)_L. \quad (28)$$

Next consider a single term in the summation in Eq. (28). In other words, consider only a single mode, say,  $L$ , propagating in the waveguide. In this particular case, we have

$$p_{\text{ih}}(\mathbf{r}) = \Lambda_L \frac{C_L}{C_L^{(0)}} \left( G^{(0)} * p^{\text{inc}} \right)_L. \quad (29)$$

It must be noted that Eq. (29) is the Born approximation of the unperturbed inhomogeneous term,  $\Lambda_L(C_L/C_L^{(0)})p$ , in the unperturbed differential equation of propagation. Therefore, the differential equation of which Eq. (29) is the Born approximation, is:

$$\left[ \nabla^2 + k_0^2 - D_L \right] p_L(\mathbf{r}) = 0, \quad (30)$$

in which

$$D_L = \Lambda_L \frac{C_L}{C_L^{(0)}}. \quad (31)$$

From Eq. (30), it follows that the phase speed for the mode under consideration in the presence of the flow is  $c_L = \omega / \sqrt{\Lambda_L^2 - D_L}$ . The contribution to the phase speed due to the flow is, therefore, the difference:

$$(\Delta c)_L = \frac{\omega}{\sqrt{\Lambda_L^2 - D_L}} - \frac{\omega}{\Lambda_L}. \quad (32)$$

Equation (32) is similar to the result which was obtained in [10] using a perturbative approach.

## 5 Numerical Computations

The details of the numerics are presented in this Section. Eigenvalues were calculated from the operator Eq. (15) which gives  $J_\ell(\kappa_L) = 0$  for the Dirichlet,  $J'_\ell(\kappa_L) = 0$  for the Neumann and  $\kappa_L J'_\ell(\kappa_L) - i\alpha R J_\ell(\kappa_L) = 0$  for the Robin boundary. Eigenvalues for the Dirichlet and Neumann cases were generated using a web interface [24] to Wolfram Research Inc.'s Mathematica software. For the Robin boundary, the eigenvalues were computed with The Mathwork's MATLAB software using Newton's method.

The corresponding normalization constants are:  $A_L = J_{\ell+1}(\kappa_L)$ ,  $A_L = J_\ell(\kappa_L) \sqrt{1 - \frac{\ell^2}{\kappa_L^2}}$ , and  $A_L = J_\ell(\kappa_L) \sqrt{1 - \frac{\ell^2 + \alpha^2 R^2}{\kappa_L^2}}$ , respectively.

Two values of the quantity,  $\zeta = |\beta|k_0 R$  namely, 0.3 and 1.2 are reported for the impedance boundary. For  $\zeta = 0.3$ ,  $\beta < \lambda/2\pi R$ , and for  $\beta$  in this range, the roots of the Robin boundary can be obtained analytically (e.g., see [16]):

$$\kappa_{00}^R = \sqrt{2iR\alpha}; \quad k_{00} = k_0 + (\beta'' + i\beta')/R, \quad (33)$$

$$\kappa_{\ell s}^R = \kappa_{\ell s}^N \left[ 1 - \frac{(\beta'' + i\beta')k_0 R}{\{\kappa_{\ell s}^N\}^2 - s^2} \right]; \quad \Lambda_{\ell s}^R = \Lambda_{\ell s}^{(0)} + \frac{(\beta'' + i\beta')k_0}{R\Lambda_{\ell s}^{(0)} \left[ 1 - \left( \frac{l}{\kappa_{\ell s}^N} \right)^2 \right]}. \quad (34)$$

Moreover,

$$\Lambda_{\ell s}^{(0)} = \sqrt{k_0^2 - \left( \frac{\kappa_{\ell s}^N}{R} \right)^2}, \quad (35)$$

and the superscripts R (N) indicates Robin (Neumann) eigenvalues, respectively. The impedance eigenvalues were calculated by numerical root finding. For  $\zeta = 0.3$ , they were identical to those computed from Eqs. (33) and (34) thereby verifying the accuracy of the root finding algorithm. However, for  $\zeta = 1.2$ ,  $\beta$  was not small compared to  $\lambda/2\pi R$ , the analytical results were not valid, and the numerical roots had to be used.

Following [11], two flow velocity distributions were considered, which were:

$$v_l(\rho) = 2\bar{v} \left( 1 - \frac{\rho^2}{R^2} \right) : \text{laminar flow}, \quad (36)$$

$$v_m(\rho) = av_l(\rho) + (1-a)v_t(\rho) : \text{a mixed laminar - turbulent flow}. \quad (37)$$

$\bar{v}$  is the mean flow speed, and the subscript  $l, m$  denote parabolic laminar and mixed flow, respectively. Moreover, again as in [11],  $a$  was:

$$a(Re) = \frac{1}{1 + \left( \frac{Re}{Re_0} \right)^n}, \quad (38)$$

where  $n = 4$ , and  $Re$  is Reynold's number:  $Re = 2\rho\bar{v}R/\mu$ ,  $\rho$ ,  $\mu$  being the fluid's mass density and viscosity, respectively.  $R = 0.006$  m in the numerics. Numerical computations were performed at the frequency of 1 MHz.

## 6 Results and Discussions

The relative changes,  $(\Delta c)_L$ , in the mode phase speeds due to flow, given in Eq. (32), constituted the primary results in this work. The profiles of  $(\Delta c)_L$  vs.  $\bar{v}$  are shown in Figs. 1 through 6, the relevant parameters in the calculations described in the figures. Considering the large amount of data (two flow profiles, three boundaries and a large  $\kappa_L$  vector with  $\ell = 0, 1$  and  $2$ , and  $s = 0, 1, 2, 3, 4$ , for each  $\ell$ ) involved, a limited, yet a representative set of results is presented. The profiles for the Dirichlet boundary are plotted in Figs. 1(a) - 1(d), and the Neumann results are displayed in Figs. 2(a) - 2(d). The data for the impedance boundary with  $\zeta = 0.3$ , are shown in Fig. 3, whereas Fig. 4 shows the same results, but for  $\zeta = 1.2$ .  $\beta$  is real in Figs. 3 and 4, imaginary  $\beta$  showing qualitatively similar variations. Moreover, Figs. 3 and 4 show the real part of  $(\Delta c)_L$ .

One distinguishing feature of the plots is that  $(\Delta c)_L$  ( $\text{Re}((\Delta c)_L)$  for the impedance condition) exhibits the same overall variation with  $\bar{v}$  for all three boundaries. If the flow is laminar,  $(\Delta c)_L$  increases linearly with mean speed for any  $L$ , whereas for the mixed flow, the increase is nonlinear. This can be understood from the following considerations. To the first-order in  $\mathbf{M}$ , a Taylor expansion of  $\sqrt{\Lambda_L^2 - D_L}$  yields:

$$(\Delta c)_L \sim \frac{D_L}{\Lambda_L^2} = \frac{1}{\Lambda_L^2} \frac{C_L}{C_L^{(0)}}, \quad (39)$$

where Eq. (31) was used. Moreover, the norm of  $(C_L/C_L^{(0)})$  reflects the norm of  $V$ , and for the laminar flow, this norm varies directly with  $\bar{v}$ . Hence, Eq. (39) results in linear variations of  $(\Delta c)_L$  with  $\bar{v}$  when the flow is laminar. For the mixed flow, however, the velocity distribution is nonlinear in  $\bar{v}$  via the factor

$a$  (see Eq. (37)), and  $a$  depends nonlinearly on  $\bar{v}$  through its dependence on Reynold's number (cf. Eq. (38)). The nonlinearity is clearly seen in all the plots for the mixed flow for all the boundary conditions considered.

The second distinguishing feature is an overall fanning out of  $(\Delta c)_L$  as  $s$  increases, all other parameters ( $\ell$ , mean flow, frequency and the waveguide) remaining constant. This follows from the fact that the eigenvalues,  $\kappa_L$ , are monotonically increasing functions of  $s$ , resulting in the decrease in the phase speed,  $\Lambda_L$ . In addition, the spread undergoes a general increase with both mode number,  $\ell$ , and mean flow. The increase with  $\ell$  follows from the interlacing property [22] of the zeros of Bessel functions, namely,  $\kappa_{\ell,1} < \kappa_{\ell+1,1} < \kappa_{\ell,2} < \kappa_{\ell+1,2} < \kappa_{\ell,3} < \dots$ . Furthermore, since  $(C_L/C_L^{(0)})$ , increases with  $\bar{v}$ , the spread of the phase speed deviations increases with the mean flow speed.

In the Robin boundary, attenuation of the waves may be expected. In other words,  $(\Delta c)_L$  may have imaginary components. It can be seen from Eq. (35) that attenuation is expected to be significant near, and of course, above the cut-off frequency of a mode. For the modes reported in this paper, the numerical calculations showed that the modes were away from their cut-off limits at the carrier frequency of 1 MHz. Attenuation was, therefore, not expected to be significant. The results of the numerical computations corroborate this, as can be seen from Fig. 4, where some typical variations of the attenuation with flow are plotted. Figure 4(a) show  $\text{Im}(\Delta c)_L$  vs.  $\bar{v}$  for  $\zeta = 0.3$ ,  $l = 0$ , and for the mixed flow. The corresponding results for  $\zeta = 1.2$  are plotted in Fig. 4(b). The attenuation is seen to be two orders of magnitude smaller than  $\text{Re}(\Delta c)_L$ . Qualitatively similar behavior was observed for the other mode numbers.  $\text{Im}(\Delta c)_L$  for  $l = 2$  in Fig. 3(b) are smaller in magnitude than those for  $l = 0$  in Fig. 3(a). This behavior was typical of  $\text{Im}(\Delta c)_L$  irrespective of



whether the flow was laminar or mixed.

We conclude our main discussions with the following remark.

**Remark:** The integral Eq. (8) is quite general, and can accommodate practical physical situations. The incident field that appears in this equation can be arbitrary, and the medium (or a part thereof) can be inhomogeneous. In the latter case, the differential Eq. (4) must be modified to:

$$\left[ \nabla^2 + k_0^2(1 + \epsilon(\mathbf{r})) + \frac{2ik_0^2}{\omega} \mathbf{V}(\mathbf{r}) \cdot \nabla \right] p(\mathbf{r}) = 0, \quad (40)$$

and the corresponding inhomogeneous part,  $p_{\text{ih}}(\mathbf{r})$ , becomes:

$$p_{\text{ih}}(\mathbf{r}) = \int_{R^1} d\mathbf{r}' G^{(0)}(\mathbf{r}|\mathbf{r}') \left[ k_0^2 \epsilon(\mathbf{r}') \chi(\mathbf{r}') + \frac{2ik_0^2}{\omega} \mathbf{V}(\mathbf{r}') \cdot \nabla \right] p(\mathbf{r}'). \quad (41)$$

In Eqs. (40) and (41),  $\epsilon$  is the medium's inhomogeneity, and  $\chi$  is the characteristic function of the compact region occupied by  $\epsilon$ . The acoustic velocity inhomogeneity is now augmented by the additional inhomogeneity,  $\epsilon(\mathbf{r}')$ , which provides physical scattering centers. Equations (40) and (41) are representatives of numerous practical engineering problems involving flow mixed with particulate matters. The above equations hold for  $\mathbf{M} < 1$ . In addition, if  $\epsilon$  is smaller than  $k_0$ , then Born approximation can be invoked. In the general case, however,  $\epsilon$  may not be small, and the second order term in the velocity may have to be incorporated. Fortunately, the integral in Eq. (41) is a convolution integral, and can be accomplished by fast solvers such as CG-FFT (conjugate gradient-fast Fourier transform) [25, 26]. Furthermore, depending upon the relative magnitudes of the velocity and the physical scattering centers, WKB type approximation can be applied.

## Acknowledgment

The authors would like to acknowledge DOD Prostate Cancer Research Program New Investigator Award No. W81XWH-04-1-0042 for support of this work.

## References

- [1] P. Mungur, H. Plumblee, Propagation and attenuation of sound in a soft walled annular duct containing shear flow, Tech. Rep. SP-207, NASA (1969).
- [2] A. H. Nayfeh, J. E. Kaiser, D. P. Telions, Acoustics of aircraft engine-duct system, AIAA 13.
- [3] M. S. Sodha, A. Kumar, J. C. Goyal, A. Ghatak, Sound wave propagation in cylindrical inhomogeneous waveguides, *Acustica* 41 (1979) 232–237.
- [4] W. Mohring, E. A. Muller, F. Obermeier, Problems in flow acoustics, *Reviews of Modern Physics* 55 (1983) 707–724.
- [5] H. Lechner, Ultrasonic flow metering based on transit time differentials which are insensitive to flow profile., *Journal of the Acoustical Society of America* 74 (1983) 955–959.
- [6] R. Astley, A finite element wave envelope formulation for acoustic radiation in moving flows, *Journal of Sound and Vibration* 103 (1985) 471–485.
- [7] N. K. Agarwall, M. Bull, Acoustic wave propagation in a pipe with fully developed turbulent flow., *Journal of Sound and Vibration* 132 (1989) 275–298.
- [8] G. R. Gogate, M. L. Munjal, Analytical solution of sound propagation in lined or unlined circular ducts with laminar flow., *Journal of Sound and Vibration* 160 (1993) 465–484.

- [9] C. Bailey, D. Juve, Numerical solutions of acoustic propagation problems using linearized euler equations, AIAA 38 (2000) 22–29.
- [10] M. Willantzen, Sound propagation in a moving fluid confined by cylindrical walls - a comparison between an exact analysis and the local-plane-wave approximation, Journal of Sound and Vibration 247 (2001) 719–729.
- [11] M. Willantzen, Perturbation theory applied to sound propagation in flowing media confined by a cylindrical waveguide, Journal of the Acoustical Society of America 109 (2001) 102–107.
- [12] S. W. Rienstra, W. Everman, A numerical comparison between the multiple-scales and finite-element solution for sound propagation in lined flow ducts, Journal of Fluid Mechanics 437 (2001) 367–384.
- [13] F. Treyssède, G. Gabard, M. Tahar, A mixed finite element method for acoustic wave propagation in moving fluids based on an eulerian- lagrangian description, Journal of the Acoustical Society of America 113 (2003) 705–716.
- [14] D. N. G. Roy, L. S. Couchman, Inverse Problems and Inverse Scattering of Plane Waves, Academic Press, London, 2002.
- [15] D. Colton, R. Kress, Inverse Acoustic and Electromagnetic Scattering Theory, Springer-Verlag, Berlin, 1992.
- [16] P. Morse, K. Ingard, Theoretical Acoustics, Princeton University Press, Princeton, 1968.
- [17] M. N. Rychagov, H. Ermert, Reconstruction of fluid motion in acoustic diffraction tomography, Journal of the Acoustical Society of America 99 (1996) 3029–3035.
- [18] S. J. Norton, Fluid flow imaging by means of wide-band diffraction tomography, Journal of the Acoustical Society of America 105 (1999) 2717–2721.

- [19] H. Braun, A. Hauck, Tomographic reconstruction of vector fields, IEEE Trans. Signal Process. 39 (1991) 464–471.
- [20] A. J. Devaney, Inverse Problems of Acoustic and Elastic Waves, SIAM, Philadelphia, 1984, Ch. Acoustic Tomography, pp. 201–227.
- [21] K. J. Langenberg, Applied inverse problems for acoustic, electromagnetic and elastic wave scattering, in: P. C. Sabatier (Ed.), Basic Methods of Tomography and Inverse Problems, Adam Hilger, Bristol, 1987, pp. 127–467.
- [22] M. Abramowitz, I. Stegun, Handbook of Mathematical Functions, US Government Printing Office, Washington, D.C., 1964.
- [23] H. F. Davis, Fourier Series and Orthogonal Functions, Allyn and Bacon, Boston, 1963.
- [24] E. Popova, Web-based computations and visualization, Web publication.  
URL <http://webcomputing.bio.bas.bg/webComputing/index.html>
- [25] X. M. Xu, Q. H. Liu, Fast spectral-domain method for acoustic scattering problems, IEEE Trans. Ultras. Ferro. Freq. Control 48 (2001) 522–529.
- [26] A. F. Peterson, R. Mitra, Method of conjugate gradient for the numerical solution of large-body electromagnetic scattering problems, Journal of the Optical Society of America A2 (1985) 971–977.

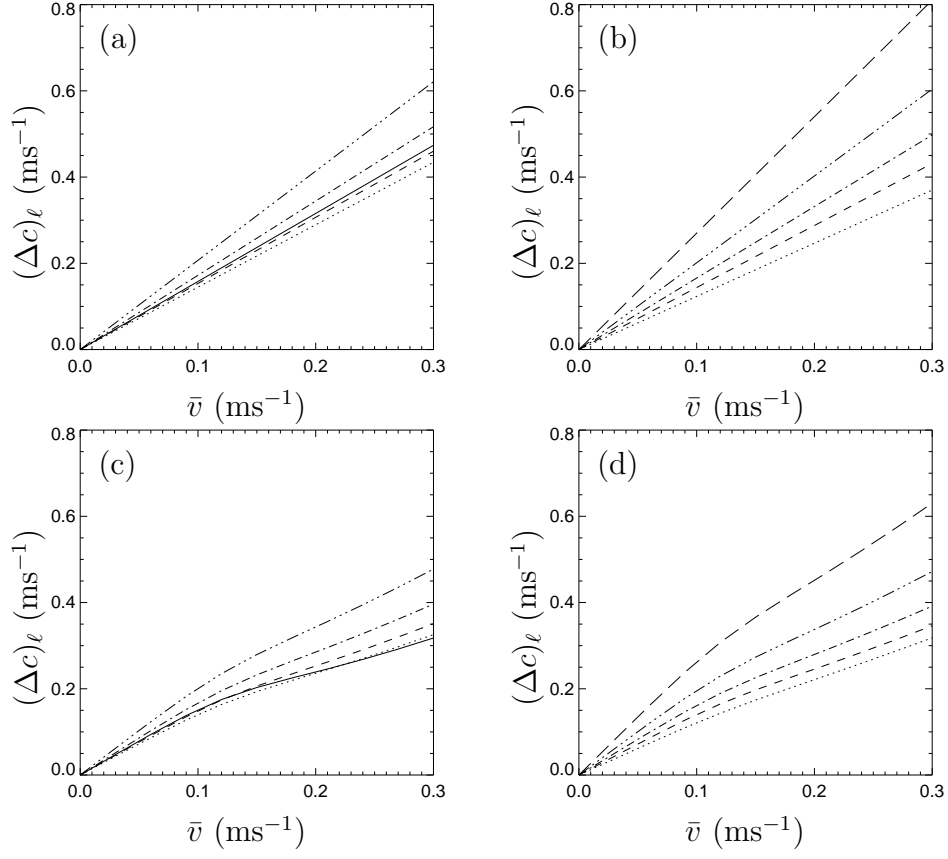


Fig. 1.  $(\Delta c)_\ell$  vs.  $\bar{v}$  for the Dirichlet boundary conditions,  $f = 1\text{MHz}$ : (a) laminar flow,  $\ell = 0$ , (b) laminar flow,  $\ell = 2$ , (c) mixed flow,  $\ell = 0$ , (d) mixed flow,  $\ell = 2$ . solid:  $s = 0$ , dot:  $s = 1$ , dash:  $s = 2$ , dash-dot:  $s = 3$ , dash-dot-dot-dot:  $s = 4$ , long-dash:  $s = 5$

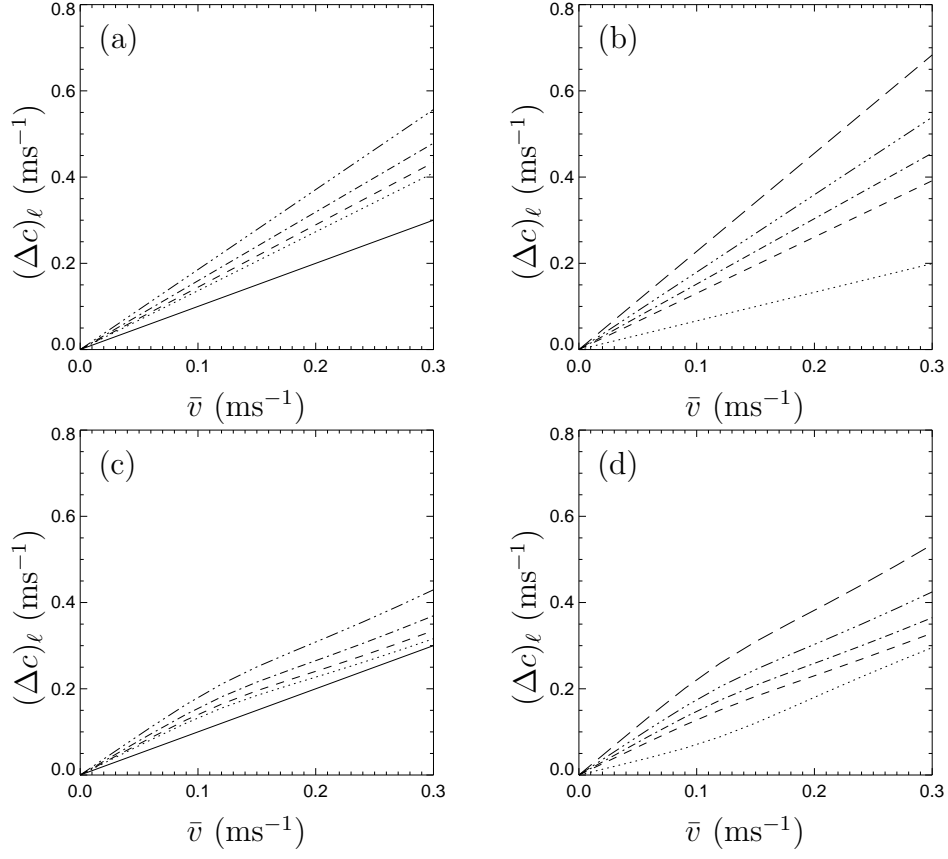


Fig. 2.  $(\Delta c)_\ell$  vs  $\bar{v}$  for the Neumann boundary conditions: (a) laminar flow,  $\ell = 0$ , (b) laminar flow,  $\ell = 2$ , (c) mixed flow,  $\ell = 0$ , (d) mixed flow,  $\ell = 2$ . solid:  $s = 0$ , dot:  $s = 1$ , dash:  $s = 2$ , dash-dot:  $s = 3$ , dash-dot-dot-dot:  $s = 4$ , long-dash:  $s = 5$

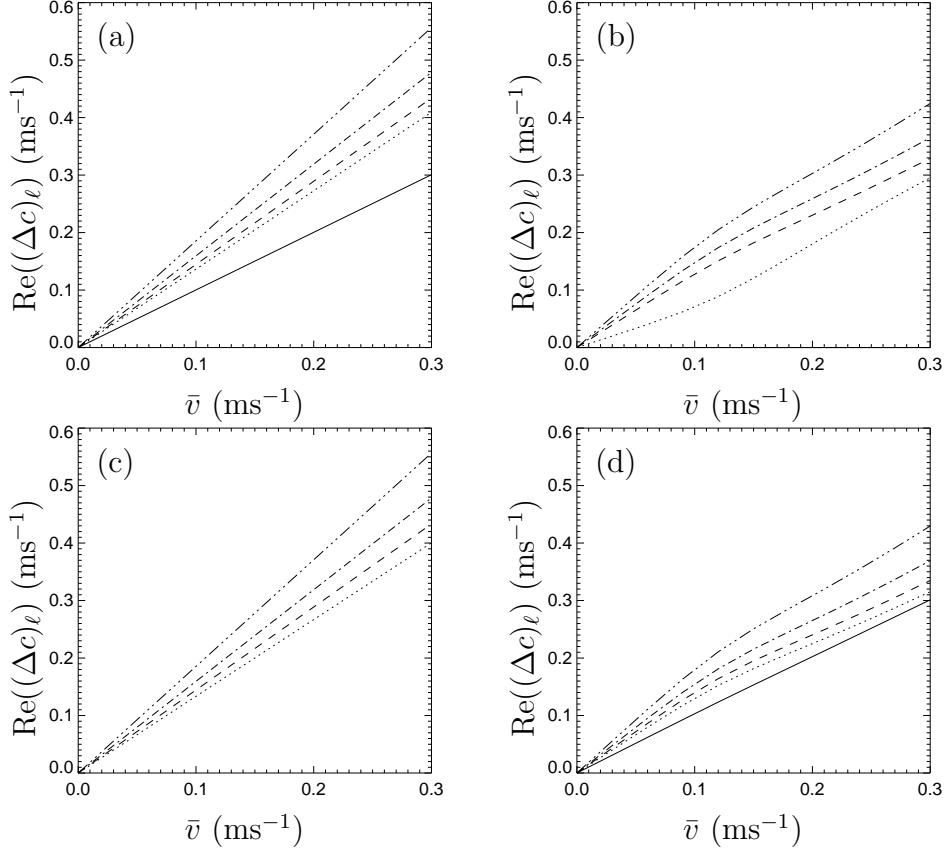


Fig. 3.  $\text{Re}(\Delta c)_\ell$  vs.  $\bar{v}$  for the Robin boundary conditions,  $f = 1\text{MHz}$ : (a)  $\zeta = 0.3$ , laminar flow,  $\ell = 0$ , (b)  $\zeta = 0.3$ , mixed flow,  $\ell = 2$  (c)  $\zeta = 1.2$ , laminar flow,  $\ell = 0$ , (d)  $\zeta = 1.2$ , mixed flow,  $\ell = 2$ . solid:  $s = 0$ , dot:  $s = 1$ , dash:  $s = 2$ , dash-dot:  $s = 3$ , dash-dot-dot-dot:  $s = 4$

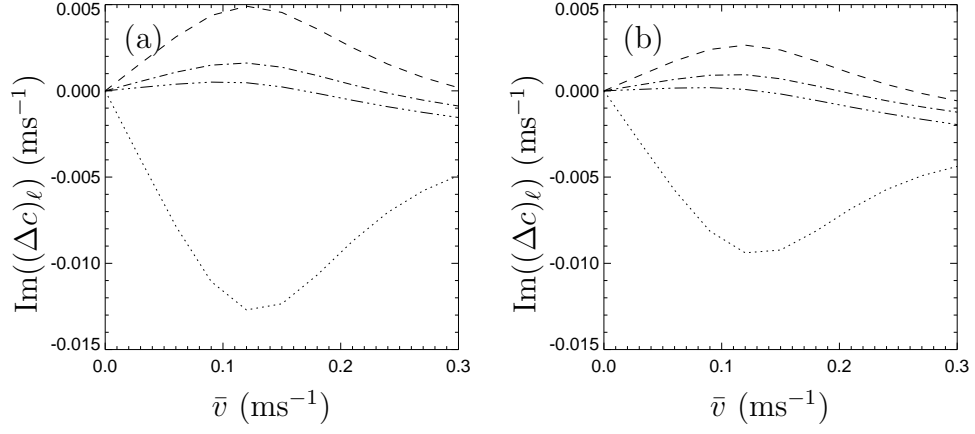


Fig. 4.  $\text{Im}(\Delta c)_\ell$  vs.  $\bar{v}$  for mixed flow with the Robin boundary conditions,  $\zeta = 1.2$ ,  $f = 1\text{MHz}$ : (a)  $\ell = 1$ , (b)  $\ell = 2$ . dot:  $s = 1$ , dash:  $s = 2$ , dash-dot:  $s = 3$ , dash-dot-dot-dot:  $s = 4$